RESEARCH MONOGRAPH · MARINE GEOLOGY & PLANETARY CRATERING MECHANICS

Re-evaluating the Miami Offshore Circular Structure: 1-Meter Multibeam Morphometry, Multi-Epoch Bathymetric LiDAR, Sub-Bottom Acoustics, Layered-Target Cratering Mechanics, and a Falsifiable Field Program

Cory Boehne · *Independent Researcher, Miami, Florida* · **Version 4.0, November 2026. Publication edition corrected November 23, 2026.**

Publication note

This independent technical paper documents seafloor rings near Government Cut, Miami. The regional geological model places porous limestone over a stronger carbonate layer. It proposes tests that could distinguish an impact in this layered target from dissolution, carbonate growth and harbor modification. This edition revises four elements of the earlier version: the treatment of historical soundings, the interpretation of a gap in the shallow acoustic reflector, the attribution of dive-plan markers and the criteria for confirming impact. The scenario model and its original weights are retained for inspection. The proposed field program has not been approved or carried out.

ABSTRACT

The Miami Offshore Circular Structure lies off Government Cut, centered at 25.749750°N, 80.122693°W, with a summit 5.39 m below Mean Lower Low Water. The regional geological model places porous Miami Limestone over a stronger carbonate unit. No core has tested this layering beneath the summit. This layered target may respond to loading differently from quartz-rich rock, and dissolution, reef and shoal growth, differential cementation and burial are all credible in it. Cory Boehne reports identifying the rings in 2012 in NOAA survey H11898. Paris, Robertson and Schwartz (2020) described fossil-bearing oolitic limestone and interpreted a solutional doline. No diagnostic shock features have been reported from their samples, which characterize only the sampled points.

Multibeam data from 2009 resolve ridges at fitted radii of 103, 187 and 270 m around a rise 1.4–1.6 m above the adjacent moat, and airborne laser surveys reproduce this relief. Within a 325 m radius, 47 soundings from 1997 closely follow the modern surface. Many of the 79 soundings from 1934–35 record smaller relief, including on today's western crests, although that survey missed the summit and recorded whole feet referenced to mean low water. A 1935 review documents dumping south of the channel. Individual load positions remain unresolved.

The published interpretation does not trace the shallow reflector across the central rise, and the summit material is unresolved. An illustrative five-hypothesis model gives impact 52.1% at an assumed 0.50% prior, with a central 90% sensitivity range of 12.8–86.2%. At a 0.10% prior, paleokarst leads. These weights depend on assigned likelihoods and model structure and are not odds that an impact occurred. At the baseline prior, I regard impact as the better-fitting single-origin working hypothesis. Harbor modification and mixed origins remain credible. No reported observation decisively rules impact out, and no site-linked diagnostic evidence confirms it. The nested arcs, central rise, northwest boulder apron and persistence across surveys warrant direct tests of the rock beneath the rings.

Keywords: impact cratering; carbonate shock metamorphism; calcite mechanical twinning; Miami Limestone; Biscayne Aquifer; eogenetic karst; multibeam bathymetry; topobathymetric LiDAR; marine geophysics; Bayesian hypothesis testing

1. Introduction and standard of evidence

Circular structures on shallow carbonate shelves can arise from multistage karst collapse, differential cementation of relict bioherms or ooid shoals, fluid or gas escape, dredge-spoil disposal or hypervelocity impact. The regional stratigraphy near Government Cut places porous Miami Limestone over a stronger carbonate unit. This layering may change the response to loading relative to quartz-rich targets, and it makes dissolution, reef and shoal growth, cementation and burial credible. A small Quaternary impact in such a setting would constrain small-body impact rates (Brown et al., 2002; Bland & Artemieva, 2006), excavation in layered targets (Quaide & Oberbeck, 1968; Ormö & Lindström, 2000; Prieur et al., 2018; Ormö et al., 2024) and shock barometry in weakly shocked carbonates (Seybold et al., 2023; Poelchau et al., 2025). Misclassification either way would distort crater-scaling databases (French & Koeberl, 2010).

The Miami Offshore Circular Structure (MOCS) lies on the shallow Atlantic inner shelf just south of Government Cut, the federal entrance channel to PortMiami in Miami-Dade County, Florida. The primary dataset is the native 1.0 m Bathymetric Attributed Grid H11898_MB_1m_MLLW_2of5.bag. Ocean Surveys, Inc. acquired it from the R/V *Able II* between March 17 and July 6, 2009, for NOAA Hydrographic Survey H11898 (Reynolds, 2009). In this grid the summit pixel of the central pinnacle lies at 25.749750°N, -80.122693°W (25°44'59.10"N, 80°07'21.69"W). In NAD83 / Universal Transverse Mercator (UTM) Zone 17N, its position is E = 587,986.16 m, N = 2,848,263.42 m. In NAD83 / Florida East State Plane (EPSG:2236), it is X = 944,933.12 USft, Y = 515,698.01 USft. The summit elevation is -5.387 ± 0.457 m relative to Mean Lower Low Water (MLLW), a water depth of 17.67 ft, with the uncertainty given as 95% total vertical uncertainty (TVU).

Distances computed as geodesics on the WGS84 ellipsoid place the summit 0.82 km (820 m) south-southwest of the Government Cut outer bar federal channel. It is 1.14 km (1,144 m) southeast of the Government Cut South Jetty tip, at an azimuth of 148.5°. It is 1.90 km (1,896 m) southeast of the Miami Beach (South Pointe) shoreline. It is also 546.9 m north of the axis of the buried Miami-Dade Central District 120-inch reinforced-concrete ocean sewer outfall pipeline. That point is 702.6 m north-northwest of exposed-pipe chart item H11898-5 at 25°44'39.170"N, 80°07'09.393"W (Reynolds, 2009).

Boehne dates his first observation in the NOAA bathymetry viewer to May 11, 2012. A contemporary image timestamp supports that date. The coordinates later published on Crater Explorer (25°44.985′N, 80°07.361′W) lie about 1 m from the summit pixel in H11898. When those precise coordinates were first recorded is unverified. In 2012 Boehne attempted to send the images to FIU geologist Dr. Grenville Draper. The May 29 email went to an address that differs from Draper's university address in the contact record. Boehne later recalled that Draper questioned a karst origin. No receipt or written assessment from Draper has been verified. In 2015 Andrew Glikson considered an impact possible under a soft-sediment interpretation and asked about the mapping and water depth. Charles O'Dale's archive also records P. V. Heinrich's comparison with circular Texas bioherms (Roberson, 1972).

Paris, Robertson and Schwartz (2020) describe a dive investigation on June 27 that sampled thirty locations, including the central area, the ridges and the northwest field. They reported fossil-bearing oolitic limestone. They observed no shatter cones or other shock features. Gauge depth at their central station was greater than at three ring stations. They proposed that uneven dissolution produced a solutional doline. These negative surface results are relevant. They do not confirm a small impact into a carbonate target, and they do not decisively eliminate one. Taylor Engineering's April 2021 report documents countywide geophysical acquisition in April 2020 and vibracoring from June 23 to July 1. The three local borings discussed in Aley's presentation were collected on June 25. Aley presented the work on February 5, 2021.

This Version 4.0 monograph supersedes the earlier qualitative preprint (Version 3.0, July 2026). It is based on a complete re-analysis of the primary federal survey and geophysical records. This version also corrects four errors carried over from Version 3.0.

First, geodetic coordinates and coastal distances now follow WGS84 geodesics computed from H11898. The summit lies 0.82 km south-southwest of the Government Cut outer bar channel, 1.14 km southeast of the South Jetty tip and 1.90 km southeast of South Beach.

Second, the spatial coverage of Aley's (2021) survey is corrected. The survey gridded MOCS Line 37 and the Eastern Outflow Lobe (Lines 31–36 and 42). It cored the eastern margin (VB-DA20-31) and the outflow lobe (VB-DA20-30). None of its tracklines, magnetic picks or vibracores entered the northwest boulder apron (H11898-28), which lay within environmental hardbottom exclusion buffers.

Third, magnetometer sensor-type labels and relative amplitude tiers have been removed because Aley's slides do not report them.

Fourth, bibliographic details are corrected. The second author of Paris, Robertson and Schwartz (2020) is R. Robertson. Seybold et al. (2023) appeared in issue 58(9), pages 1287–1305. Meyer, Harries and Portell (2019) appeared in 54(7), pages 1594–1603, and the description of its Plio-Pleistocene chronostratigraphic separation is corrected.

Paris et al. (2020) found fossil-bearing oolitic limestone at the sampled points, with no diagnostic shock evidence reported. Morphology alone cannot settle the origin, since a mound can rise from a basin floor and carbonate dredge material can overlie natural hardbottom. Under the baseline assumptions of section 9, impact is the better-fitting single origin at a 0.50% prior, while paleokarst leads at 0.10%. Eogenetic karst, bioherms and ooid shoals (Roberson, 1972), documented dumping and mixed origins remain credible. Section 10 proposes summit-crossing sub-bottom profiles, cores into the stronger lower unit, petrography of suitable grains for diagnostic shock features and controlled tests for projectile contamination. Calcite twinning alone would not establish impact. These results matter because each origin predicts different material beneath the summit.

> **Terminology: Bathymetric Ring R1 and Sub-Bottom Reflector R1**
>
> Two different features carry the label R1 in earlier datasets. This paper distinguishes them as follows.
>
> 1. Bathymetric inner ring (Ring R1). This is the innermost concentric seabed ridge of MOCS. Its fitted circle has radius R = 102.56 m and diameter 2R = 205.11 m, within a radial search zone of 68–128 m. Moving outward, it is followed by the bathymetric middle ring (Ring R2, R = 187.37 m) and the bathymetric outer ring (Ring R3, R = 270.26 m).
> 2. Sub-bottom acoustic reflector (Reflector R1). This is the shallow contact picked in red on Aley's acoustic profiles. It may mark rock or gravel. Where the pick stops, its geometry, lateral continuity and relationship to deeper bedrock remain unresolved.

2. Geological, stratigraphic and hydrodynamic setting

2.1 Four-layer Biscayne Aquifer target stratigraphy off Government Cut

Southeastern Florida lies on a passive-margin carbonate ramp. No Quaternary faulting, volcanism, evaporite diapirism or tectonic folding is documented there (Hoffmeister, 1974). The coastal Biscayne Aquifer underlies the inner shelf off Miami Beach, Fisher Island and Virginia Key. High-resolution coreholes and borehole geophysical logs from this aquifer show a layered sequence of Neogene–Quaternary carbonates and siliciclastics (Hoffmeister, Stockman, & Multer, 1967; Perkins, 1977; Halley & Evans, 1983; Fish & Stewart, 1991; Cunningham et al., 2006, 2009; Neal et al., 2008). Table 1 summarizes the local four-layer column beneath MOCS, where present water depth is 5.4–7.0 m MLLW (mean lower low water). The column is generalized. Porosity, cementation and unit thickness vary over short distances in these carbonates, and the properties at the site itself have not been sampled.

This host is relevant to the origin question in two ways. The target is shallow, porous and mechanically layered, with weak, porous Miami Limestone resting on a stronger carbonate unit. Such a target can respond to loading differently from the quartz-rich targets that dominate the cratering literature, so an independently diagnosed impact here would show how a small shallow-marine event in layered carbonate might be recognized. The same rocks also host carbonate dissolution, reef and shoal growth, differential cementation and burial. Table 1 therefore serves as the target stratigraphy for the impact models and also constrains the dissolution, karst, reef, shoal and harbor-modification hypotheses.

Table 1. Local four-layer lithostratigraphic and mechanical column of the Biscayne Aquifer off Government Cut, Miami-Dade County, Florida, used as the target column in the impact models (compiled from Hoffmeister et al., 1967; Fish & Stewart, 1991; Cunningham et al., 2006, 2009).

Layer	Stratigraphic Unit & Chronostratigraphy	Local Thickness H_i (m)	Subseafloor Depth z (m)	Total Porosity ϕ (%)	Bulk Density ρ (kg m^{-3})	Lab UCS q_u / Cratering Yield Y_{eff} (MPa)	V_p (m s^{-1}) / Acoustic Impedance Z (MRayl)
0	**Atlantic Inner-Shelf Water** *(0 m during MIS 4–2 glacial lowstand; 3–12 m in MIS 5a/c or mid-to-late Holocene)*	0 *(lowstand)*; 3–12 *(nom. 8.0)*	-8 to 0	—	1,025	0 / 0	1,530 / 1.57
1	**Miami Limestone** *(Upper cross-bedded oolitic facies & lower touching-vug bryozoan facies; MIS 5e, ~120–130 ka)*	8–15 *(nominal 12.0)*	0 to 12	30–45	2,000 *(sat.)*	1.5–5.0 *(med. ~3)* / **0.45**	2,100 / **4.20**
2	**Fort Thompson Formation** *(Cyclostratigraphic dense marine/freshwater limestones + laminated exposure calcretes; MIS 11–7, ~420–200 ka)*	15–25 *(nominal 20.0)*	12 to 32	15–30	2,400	8.0–32.0 / **14.0**	3,500 / **8.40**
3	**Upper Tamiami Formation (Pinecrest Beds)** *(Shelly calcarenite, moldic limestone & quartzose sand; Plio-Pleistocene, ~2.0–3.2 Ma)*	18–26 *(nominal 22.0)*	32 to 54	22–35	2,250	3.0–12.0 / **4.5**	2,700 / **6.08**
4	**Hawthorn Group** *(Peace River / Arcadia dolosilts & clays forming the confining base of the Biscayne Aquifer; Oligocene–Pliocene)*	>100 *(100–220)*	>54	20–32	2,350	5.0–20.0 / **10.0**	3,000 / **7.05**

Three stratigraphic and petrophysical conditions in Table 1 constrain each origin hypothesis evaluated below:

1. Strong mechanical contrast near $z \approx 12$ m below the seafloor. The uppermost unit is the MIS 5e Miami Limestone (~120–130 ka; Osmond, Carpenter, & Windom, 1965; Muhs et al., 2011), a coastal barrier-shoal wedge about 12 m thick. Its porosity of 30%–45% includes intergranular pores, oomolds (voids left by dissolved ooids) and large interconnected vugs formed along burrows. Meniscus and sparry calcite cements are weak. Unconfined compressive strength (UCS) is 1.5–5.0 MPa, the assigned rock-mass cratering yield strength is $Y_1 \approx 0.45$ MPa, and acoustic impedance is $Z_1 = 4.20$ MRayl (Cunningham et al., 2006, 2009). The Sangamonian basal unconformity of the Miami Limestone lies at $z \approx 8$–15 m along the Miami Beach–Virginia Key barrier axis (Fish & Stewart, 1991). Below it lies the Middle Pleistocene Fort Thompson Formation (MIS 11–7), which consists of densely cemented marine and freshwater limestones with several laminated calcretes capping subaerial exposure surfaces (the Q-horizons of Perkins, 1977). UCS rises to 8.0–32.0 MPa ($Y_2 \approx 14.0$ MPa), and impedance rises to $Z_2 = 8.40$ MRayl. With the nominal values in Table 1, effective rock-mass yield strength increases about 30-fold across the boundary and acoustic impedance doubles. The depth of the unconformity and the degree of cementation on either side may differ at the site. A contrast of this size can control where excavation, dissolution, collapse or differential cementation stops, so it bears on every hypothesis considered here.
2. Nearly pure carbonate mineralogy and age separation from the Tamiami microtektites. Regional descriptions of the oolitic and bryozoan lithofacies of the Miami Limestone report >95–98 wt% $CaCO_3$. The originally aragonitic ooids partially inverted to low-Mg meteoric calcite spar during Wisconsinan exposure and were cemented by marine and vadose calcite (Hoffmeister et al., 1967; Halley & Evans, 1983). These regional descriptions put detrital quartz at <1–3 wt%. They do not give mineral percentages for the 30 dive specimens. The quartz occurs as silt to very fine sand grains in ooid nuclei. This composition limits the silicate phases available to record shock metamorphism. A shock search would therefore need to target those sparse grains with mineral-specific diagnostic criteria, paired with carefully controlled geochemistry. Calcite twinning alone would not establish an impact origin. Layer 3 (z = 32–54 m) corresponds to the Pinecrest beds of the Upper Tamiami Formation (Plio-Pleistocene, ~2.0–3.2 Ma). Meyer, Harries, & Portell (2019, pp. 1594–1603) reported translucent glassy microtektites from this unit inside articulated *Mercenaria campechiensis* shells in southwestern Florida. About 20 m of Middle Pleistocene Fort Thompson strata separate the Pinecrest beds from the <130 ka MIS 5e Miami Limestone, an age gap of >1.8 Myr. The microtektite

horizon is therefore far older than any event that disrupted the Miami Limestone and provides no evidence on the formation of MOCS.

3. Sea-level window after 130 ka. The Miami Limestone accumulated during the MIS 5e interglacial highstand, when sea level stood ~+6 m above modern mean sea level (MSL; Muhs et al., 2011). Any event that disrupted it must be younger than the unit, although the age of the present surface morphology is not constrained. The impact scenarios consider two environmental end-members:

(a) Subaerial formation (H_w = 0 m) during the MIS 4–2 Wisconsinan glacial lowstand (~75–15 ka), when sea level fell as much as 120 m below modern MSL and exposed the whole Florida shelf to meteoric vadose and phreatic diagenesis.

(b) Formation under shallow inner-shelf water (H_w = 3–12 m, nominal 8 m) during late MIS 5 substages (~110–80 ka) or during the mid-to-late Holocene transgression (<8 ka).

The same history bears on the alternatives. Lowstand exposure would have favored meteoric dissolution and karst, and later submergence would have allowed reef growth, shoal migration and burial.

2.2 Geodetic frame and vertical datum transformations (MLLW and NAVD88)

The study compares NOAA hydrographic surveys referenced to MLLW, airborne topobathymetric LiDAR referenced to the North American Vertical Datum of 1988 (NAVD88), and Bureau of Ocean Energy Management (BOEM) vibracores referenced to NAVD88 in US survey feet. These data sets must be converted to a common vertical datum. Survey H11898 is controlled by NOAA National Water Level Observation Network (NWLON) Station 8723214 at Virginia Key, Biscayne Bay (25.7314°N, -80.1618°W), on the 1983–2001 National Tidal Datum Epoch (Reynolds, 2009; NOAA CO-OPS, 2020). The published tidal offsets at this station are NAVD88 − MLLW = +0.614 m ($Z_{\mathrm{MLLW}} = Z_{\mathrm{NAVD88}} + 0.614$ m), MSL − MLLW = +0.342 m, MHW − MLLW = +0.661 m (mean high water) and MHHW − MLLW = +0.683 m (mean higher high water). MOCS (25.7498°N, -80.1227°W) lies seaward of Bear Cut and Government Cut. The tidal range there is not attenuated by the inlets. At this site, NOAA VDatum (NAD83_2011 / GEOID18) gives NAVD88 − MLLW = +0.691 ± 0.077 m. Over MOCS, 353,721 bedrock pixels at 1 m resolution overlap in both data types. The median differences between NAVD88 LiDAR grids and MLLW multibeam soundings are -0.557 m for the 2016 US Army Corps of Engineers National Coastal Mapping Program (USACE NCMP) survey and -0.639 m for the 2018–2019 NOAA National Geodetic Survey (NGS) survey. These two medians bracket the Virginia Key tie (-0.614 m) and lie within 2.5–5.7 cm of it. The 2018–2019 median also falls within the ±0.077 m uncertainty of the VDatum tie (-0.691 m), whereas the 2016 median falls outside it. Both medians lie well inside the ±0.457 m error budget for International Hydrographic Organization (IHO) Order 1 total vertical uncertainty at 95% confidence.

3. Geomorphometry from 1 m multibeam data, concentric rings and volume balance

3.1 Regional inner-shelf trend plane and central rise relief

The Miami–Biscayne carbonate ramp slopes gently seaward. To separate local structural relief from that slope, all datasets were projected onto a common 1.0 × 1.0 m grid in NAD83 / UTM Zone 17N (EPSG:26917). The grid is centered on the elevation-weighted centroid of the Central Rise edifice at 25.749781°N, -80.122655°W (E_0 = 587,989.92 m, N_0 = 2,848,266.84 m). The basal footprint of the edifice, defined as cells with $r \leq 20$ m and $Z > -6.40$ m MLLW, covers A = 541 m², which corresponds to an effective basal diameter of about 26.2 m. The regional carbonate shelf background plane was fitted by iterative ordinary least squares with 2.5σ clipping. The fit used n = 702,315 control shelf cells at 1-m resolution that were interpreted as unmodified. These cells lie west of MOCS, south of MOCS (seaward of the H11898-5 outfall trench) and north-northeast of MOCS. The root-mean-square (RMS) residual of the fit is 0.152 m:

$$Z_{\mathrm{bg}}(E,N) = (-1.455\ \mathrm{m\ km^{-1}})\Delta E_{\mathrm{km}} + (-0.199\ \mathrm{m\ km^{-1}})\Delta N_{\mathrm{km}} - 6.615\ \mathrm{m\ MLLW} \quad (1)$$

where ΔE_{km} = (E - 587,989.92)/1000 and ΔN_{km} = (N - 2,848,266.84)/1000. The reference inner shelf dips seaward at 1.468 m/km (0.0841°) toward azimuth 082.2° (E/ENE). It passes through -6.615 m MLLW beneath the center of MOCS (Figure 1A). The detrended residual elevation is $\Delta Z = Z - Z_{bg}$. Across the southwest shelf sector (180°–270°, r = 250–415 m), ΔZ averages -0.02 ± 0.02 m. In that sector, the plane therefore shows no bias larger than a few centimeters.

The Central Rise is enclosed by an annular Inner Moat (r = 18–52 m, area 7,185 m²). The moat floor has a mean of -6.577 m, a median of -6.625 m and a 5th percentile (p05) of -6.793 m, with a deepest pixel of -6.945 m MLLW. The Central Rise summit lies at -5.387 ± 0.457 m MLLW. It stands +1.41 m above the p05 moat floor, +1.56 m above the deepest moat cell and +1.22 m above the regional shelf background plane (Figure 1B, Figure 2A).

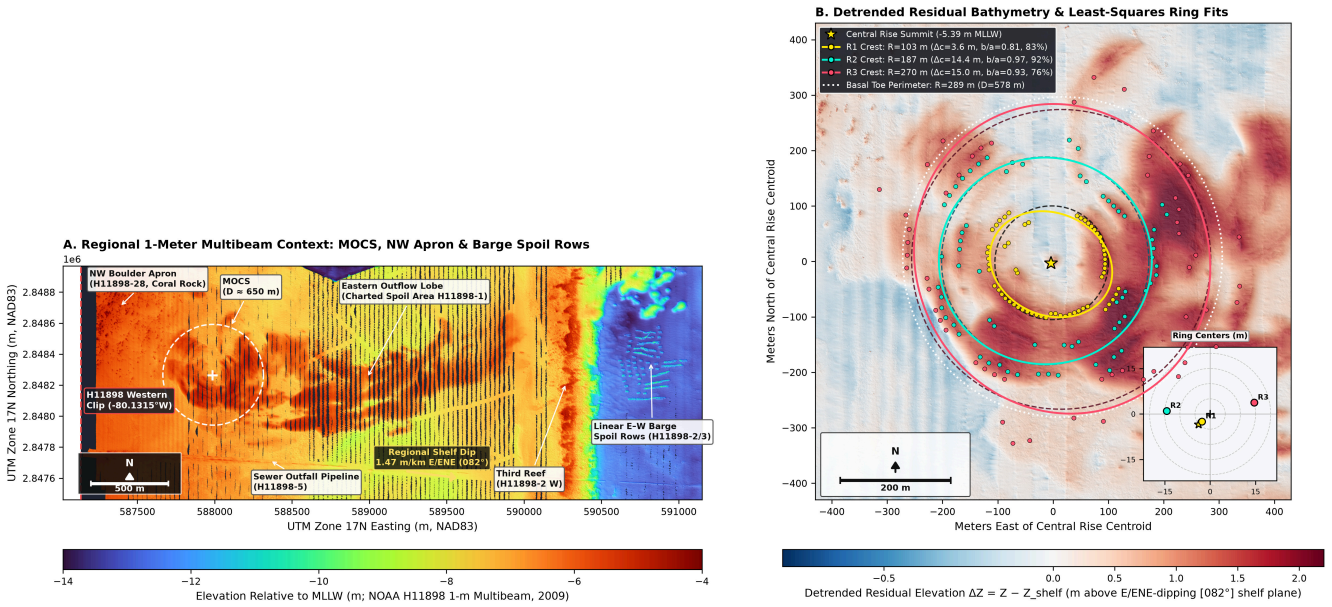

Figure 1. Regional 1.0-m multibeam bathymetry (NOAA Survey H11898, March–July 2009; Reynolds, 2009) and detrended concentric ring architecture of the Miami Offshore Circular Structure (MOCS). **(A)** Regional elevation map in NAD83 / UTM Zone 17N (m MLLW). The map shows MOCS ($D \approx 650$ m) and the coral-colonized calcareous NW Boulder Apron (H11898-28). In H11898 the apron is cut off on the west at -80.1315°W, the planned junction with the LiDAR survey. Also shown are the Eastern Outflow Lobe inside the Spoil Area designated on NOAA Chart 11468 (H11898-1), the Miami-Dade 120-inch sewer outfall pipeline (H11898-5, 546.9 m S of the summit) and linear spoil rows attributed to split-hull scow barge disposal (H11898-2/3) seaward of the Third Reef. **(B)** Detrended residual relief $\Delta Z = Z - Z_{bg}$ above the regional shelf plane, which dips 1.47 m/km toward 082.2° (E/ENE) (Eq. 1). Overlays show polar crest detections in 5° sectors (72 sectors) and least-squares circle and ellipse fits. The fitted features are Bathymetric Ring R1 (R = 102.6 m), Ring R2 (R = 187.4 m), Ring R3 (R = 270.3 m) and the outer basal edifice perimeter (R = 288.8 m, 2R = 577.5 m). The lower-right inset shows the offsets of the ring centers (Δc = 3.6–15.0 m) from the Central Rise summit (star).

3.2 Concentric ring fitting, seven-domain geomorphometry and harmonic spectrum

Radial crest detection was automated in 5° sectors (72 azimuthal sectors) on $\Delta Z(r, \theta)$. Two fits were applied to the detected crests. The first was an algebraic least-squares circle with 95% confidence intervals (CIs) from 1,000 bootstrap trials. The second was a direct Fitzgibbon ellipse. The fits identify three nested, concentric bathymetric rings of positive relief (Table 2, Figure 1B):

- Bathymetric Inner Ring (Ring R1, r = 68–128 m): The best-fit circle has radius R = 102.56 m (95% CI: 98.9–106.3 m, 2R = 205.11 m). Its center is offset by Δc = 3.64 m (3.55% of R1) from the Central Rise centroid. Crests were detected in 60 of 72 sectors, an azimuthal completeness of 83.3%. The best-fit ellipse measures 113.46 × 92.15 m, with aspect ratio b/a = 0.812 and a major axis striking 112.7° (WNW–ESE).
- Bathymetric Middle Ring (Ring R2, r = 135–222 m): The circle radius is R = 187.37 m (95% CI: 181.0–193.7 m, 2R = 374.75 m). The center offset is Δc = 14.41 m (7.69%). Crests were detected in 66 of 72 sectors, an azimuthal completeness of 91.7%. The ellipse is close to circular, at 192.41 × 186.37 m (b/a = 0.969).

- Bathymetric Outer Ring Crest (Ring R3, r = 230–340 m) and Basal Edifice Perimeter: The circle radius is R = 270.26 m (95% CI: 261.0–279.5 m, 2R = 540.52 m). The center offset is Δc = 15.01 m (5.56%). Crests were detected in 55 of 72 sectors, an azimuthal completeness of 76.4%. The ellipse measures 283.19 × 263.61 m (b/a = 0.931). The outer basal toe of the edifice was traced at $\Delta Z = +0.22$ m, excluding the 65°–125° ENE corridor where the edifice merges with the lobe. This trace gives a circle of R = 288.75 m (2R = 577.50 m) and an ellipse major axis of 2a = 682.8 m. Boehne & O'Dale (2012) and later descriptions report a visual outer footprint of about 580–650 m. The basal toe fit lies within that range and explains most of the difference between that footprint and the 540.5 m outer ring crest.

Table 2. Least-squares circle fits (95% CI from 1,000 bootstrap trials) and Fitzgibbon ellipse fits to the bathymetric ring crests of MOCS, detected in 5° sectors (72 sectors), and to the outer basal edifice perimeter (H11898 1.0-m multibeam).

Bathymetric Ring / Horizon	Radial Search Zone (m)	Azimuthal Completeness	Circle Radius R (95% CI, m)	Circle Diameter 2R (m)	Radial RMSE (m)	Center Offset Δc (m / %R)	Ellipse Semi-Axes $a \times b$ (m)	Aspect Ratio b/a (Eccentricity e)	Major-Axis Strike (° E of N)
Inner Ring (Ring R1)	68–128	**83.3%** (60/72)	**102.56** (98.9–106.3)	**205.11**	13.50	**3.64 m (3.55%)**	113.46 × 92.15	0.812 (0.584)	**112.7°** *(WNW–ESE)*
Middle Ring (Ring R2)	135–222	**91.7%** (66/72)	**187.37** (181.0–193.7)	**374.75**	26.05	**14.41 m (7.69%)**	192.41 × 186.37	**0.969** (0.249)	90.6° *(E–W)*
Outer Ring Crest (Ring R3)	230–340	**76.4%** (55/72)	**270.26** (261.0–279.5)	**540.52**	36.22	**15.01 m (5.56%)**	283.19 × 263.61	0.931 (0.365)	152.9° *(NNW–SSE)*
Outer Basal Edifice Toe	240–385*	91.5% (54/59)*	**288.75** (275.3–300.9)	**577.50**	46.73	18.80 m (6.51%)	341.38 × 273.15	0.800 (0.600)	31.5°

**Evaluated at $\Delta Z = +0.22$ m, outside the 65°–125° ENE sector where the outflow lobe and spoil merge with the edifice ($2a$ = 682.8 m).*

Table 3 compares the seven geomorphic sub-domains with the unmodified shelf control. The compared metrics are Horn slope on a 3 × 3 m window, Fine (3–15 m) and Broad (15–75 m) Bathymetric Position Indices (BPI), RMS surface roughness on a 5 × 5 m window, and orientation coherency from a 2D structure tensor.

Table 3. Geomorphometric comparison of the MOCS structural zones, the NW Boulder Apron (H11898-28), the Eastern Outflow Lobe (H11898-1), the linear barge spoil rows (H11898-2/3) and the unmodified control shelf.

Geomorphic Domain	Valid Area (m^2)	Z_{MLLW} [Min, Max] (Med, m)	Residual ΔZ Med / p95 / Max (m)	Slope Med / p90 / p99 (°)	Fine BPI [p05, p95] (Max, m)	5×5 m RMS Rough. Med / p95 (cm)	Orientation Coherency (Strike °)
(i) Central Rise (r ≤ 18 m)	975	[-6.82, -5.39] (-6.36)	+0.26 / +0.93 / **+1.22**	3.57° / 6.15° / 9.26°	[-0.14, +0.48] (+0.81)	9.0 / 15.8	0.074 (91.2°)
(ii) Inner Moat (r = 18–52 m)	7,185	[-6.95, -5.62] (-6.62)	0.00 / +0.41 / +1.06	1.23° / 2.87° / 6.26°	[-0.15, +0.06] (+0.42)	3.0 / 8.3	0.357 (168.1°)
(iii) Bathymetric Ring R1 (68–128 m)	26,452	[-6.59, -4.27] (-5.50)	+1.10 / +1.80 / +2.24	1.65° / 3.43° / 5.87°	[-0.13, +0.18] (+0.89)	3.9 / 9.0	0.264 (135.9°)
(iv-a) Bathymetric Ring R2 (135–222 m)	71,444	[-6.68, -4.18] (-5.38)	+1.23 / +2.09 / **+2.60**	1.57° / 3.29° / 5.46°	[-0.12, +0.17] (+0.54)	3.7 / 8.6	0.116 (5.6°)
(iv-b) Bathymetric Ring R3 (230–335 m)	120,768	[-6.95, -4.40] (-5.87)	+0.73 / +1.90 / +2.56	1.47° / 3.01° / 5.10°	[-0.11, +0.12] (+1.33)	3.4 / 7.6	0.153 (138.5°)
(v-a) NW Boulder Apron (H11898 E of clip)	230,265	[-6.53, -2.77] (-5.61)	+0.33 / +1.00 / +2.94	1.13° / **8.28°** / **22.50°**	[-0.22, +0.34] (**+2.00**)	3.3 / **24.3**	**0.217** (26.0°)*
(v-b) NW Boulder Apron (Full 1-m LiDAR)	452,783	[-6.44, -2.21] (-5.27)	+0.36 / +2.33 / +2.89	1.67° / 5.69° / 17.48°	[-0.18, +0.24] (+1.92)	3.4 / **19.4**	**0.236** (22.5°)
(vi) Eastern Outflow Lobe (H11898-1)	773,312	[-8.69, -4.67] (-6.82)	+1.39 / +2.73 / +3.55	1.08° / 3.10° / 6.37°	[-0.12, +0.12] (+1.02)	2.5 / 9.5	0.434 (80.0°)
(vii-a) Linear E–W Barge Rows (H11898-2)	234,876	[-13.95, -8.48] (-13.10)	-2.33† / -0.86 / +2.33	0.92° / **20.26°** / **41.49°**	[-0.51, +0.94] (**+3.97**)	2.1 / **60.7**	**0.631 (87.6°)**
(viii) Comparison Shelf (modern reference area)	702,315	[-8.22, -5.05] (-6.13)	-0.01 / +0.28 / +0.44	0.87° / 2.55° / 6.07°	[-0.08, +0.07] (+0.81)	2.1 / 6.3	0.067 (80.8°)

**Structure-tensor coherency for (v-a) was evaluated on the gap-free 2019 1-m LiDAR to avoid N–S swath-edge artifacts in the multibeam data. †H11898-2 lies in the outer inter-reef trough seaward of the Third Reef, at -13.1 m MLLW. There, individual ridges attributed to scow loads stand +2.5 to +5.5 m above the local floor at -13.5 m.*

3.3 Azimuthal harmonics and residual volume balance

The detrended relief was decomposed into azimuthal Fourier harmonics (m = 0, 1, 2, 3, 4) and integrated by volume (Figure 2B–D). Two geometric results follow.

1. Concentric (m = 0) component with a superimposed WNW–ESE (m = 1) component. Across r = 60–230 m, the axisymmetric ring harmonic ($|A_0|$ = 0.50–1.12 m) exceeds all higher-order terms (m = 2, 3, 4 < 0.45 m). This indicates that the rings are organized around a common center to first order, for the center used in the decomposition. A coherent WNW–ESE dipole (A_1 = 0.55–0.94 m) is superimposed on the m = 0 term. In the southeastern quadrant (90°–180°), the ring crests are prominent (ΔZ_{SE} = +1.91 m mean) and shoal to -4.18 m MLLW. In the northwestern quadrant (270°–360°), ring relief is subdued (ΔZ_{NW} = +0.36 to +0.60 m). The relief is lowest along 293° WNW, in the direction of the NW Boulder Apron. This direction is collinear with the 112.7° / 292.7° major axis of Ring R1 (Figure 2B–C).
2. Net positive relief within the footprint. Integrating ΔZ across the nominal 650 m footprint (R ≤ 325 m, 331,836 m²) gives V_+ = +264,766 m³ above the regional shelf plane and V_− = −7,370 m³ below it. The net volume is V_{net} = +257,396 m³, with a sensitivity range of [+207,620, +307,171] m³ for Z_{bg} ± 0.15 m. Restricted to the western semicircle (180°–360°), the net volume is +81,975 m³ (Figure 2D).

The result does not match a simple recessed dissolution bowl, which would give a net negative volume relative to the shelf plane. It does not exclude dissolution combined with residual highs or later infill, and it is also compatible with reef or shoal growth or with added material. The modern western quadrant provides a useful geometric comparison, but historical disturbance or deposition there cannot be excluded. A positive volume describes the shape relative to the fitted plane. It does not identify the material or its origin.

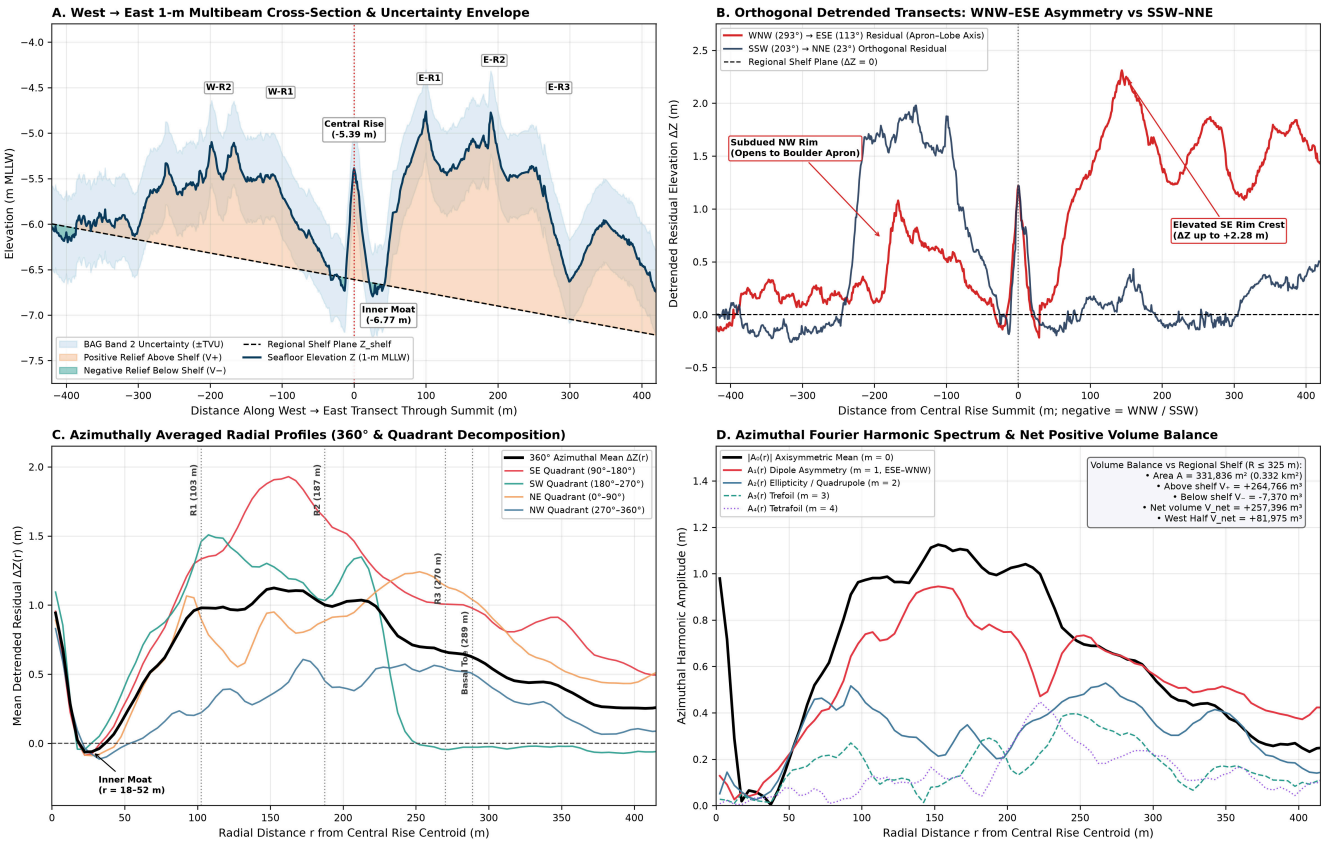

Figure 2. Directional cross-sections, quadrant radial profiles, azimuthal Fourier harmonics, and net volume balance of MOCS (NOAA H11898 1-m multibeam). **(A)** West-to-east transect through the Central Rise summit (-5.387 m MLLW). The transect shows the 95% total vertical uncertainty (TVU) Band 2 envelope (±0.457 m), the Inner Moat (-6.77 m along the slice), Bathymetric Rings R1–R3, and the regional shelf trend plane dipping toward 082.2°. **(B)** Orthogonal detrended transects along the 293°→113° WNW–ESE apron-to-lobe axis (red) and the 203°→023° SSW–NNE axis (blue). SE rim relief reaches ΔZ = +2.28 m. NW rim relief is subdued where the rim opens toward the boulder apron. **(C)** 360° mean and quadrant radial profiles, showing the return to ΔZ ≈ 0 across the SW shelf beyond r = 250 m. **(D)** Azimuthal Fourier harmonic amplitudes ($m = 0..4$) and volume summary (V_net = +257,396 m³ total, +81,975 m³ in the West Half).

4. Multi-epoch topobathymetric LiDAR and the northwest boulder apron

4.1 Historical soundings and survey repeatability across Hurricane Irma

At 4.2–7.0 m water depth on a coast exposed to hurricanes, any candidate seabed feature must be tested against two artifacts unrelated to bedrock. The first is survey error, such as multibeam swath or refraction errors. The second is the migration of mobile sand waves or unconsolidated spoil. Hurricane Irma affected southeast Florida on September 10, 2017. The surveys bracket the storm, but this study did not measure local seabed forces. Nine bathymetric datasets spanning 1928–2019 were evaluated. The 2009 H11898 1.0-m acoustic multibeam survey was co-registered with five independent airborne green-laser (532 nm) topobathymetric LiDAR surveys. These are the 2008 NOAA/JALBTCX H11870 3-m survey, the 2016 USACE NCMP 1-m pre-Irma survey, the 2017 FEMA/USACE 1-m post-Irma survey, the 2017 NOAA NGS 1-m survey, and the 2018–2019 NOAA NGS 1-m post-Irma survey (JALBTCX, 2008; USACE/JALBTCX, 2016; USACE/FEMA, 2017; NOAA NGS, 2017, 2019) (**Table 4**, **Figure 3**).

Table 4. Cross-sensor elevation repeatability between acoustic multibeam (2009 H11898) and airborne 532 nm topobathymetric LiDAR (2008–2019), and between pre- and post-Irma LiDAR epochs, across MOCS (R ≤ 350 m) and the NW Boulder Apron (H11898-28). The standard deviation of the elevation difference is reported after the listed datum tie and removal of the mean offset.

Epoch Comparison Pair	Spatial Footprint	Overlapping 1-m Cells (n)	Datum Tie Applied (m)	Median ΔZ (m)	Demeaned $\sigma_{\Delta Z}$ (m)	Interquartile Range IQR (m)	Elevation Pearson r	Fine-BPI Pearson r
2008 H11870 (3-m LiDAR) – 2009 H11898 (1-m MBES)	MOCS (R ≤ 350 m)	353,721	0.000	+0.196	**0.081**	0.105	**0.9914**	—
2016 USACE NCMP (1-m Pre-Irma) – 2009 H11898	**MOCS (R ≤ 350 m)**	**353,721**	**+0.614**	**+0.057**	**0.062**	**0.080**	**0.9948**	0.5286
2017 FEMA/USACE (1-m Post-Irma) – 2009 H11898	MOCS (R ≤ 350 m)	170,718	+0.614	+0.091	**0.090**	0.109	**0.9867**	0.4683
2017 NOAA NGS (1-m) – 2009 H11898	MOCS (R ≤ 350 m)	136,826	+0.691	-0.135	**0.071**	0.091	**0.9885**	—
2018–19 NOAA NGS (1-m Post-Irma) – 2009 H11898	**MOCS (R ≤ 350 m)**	**353,721**	**+0.614**	**-0.026**	**0.104**	**0.126**	**0.9855**	0.4493
2018–19 NGS (Post-Irma) – 2016 USACE (Pre-Irma)	**MOCS (R ≤ 350 m)**	**384,855**	**0.000**	**-0.081**	**0.082**	**0.099**	**0.9912**	**0.7284**
2018–19 NGS (Post-Irma) – 2016 USACE (Pre-Irma)	NW Apron (E of clip)	267,500	0.000	-0.102	**0.079**	0.074	0.9830	**0.9149**
2018–19 NGS (Post-Irma) – 2016 USACE (Pre-Irma)	NW Apron (W of clip)	177,951	0.000	-0.119	**0.057**	0.062	**0.9987**	**0.8974**

Across n = 353,721 co-located 1-m MOCS cells, the 2016 USACE LiDAR matches the 2009 H11898 multibeam with a demeaned σ_ΔZ of 0.062 m (IQR = 0.080 m, r = 0.9948). The post-Irma 2018–2019 NOAA NGS LiDAR matches H11898 with σ_ΔZ = 0.104 m (IQR = 0.126 m, r = 0.9855). The two LiDAR epochs that bracket Irma agree with each other at σ_ΔZ = 0.082 m and r = 0.9912 (n = 384,855) (**Figure 3C–D**).

Fine-scale relief agrees less closely than elevation. Fine-BPI r is 0.7284 between the 2018–19 and 2016 LiDAR surveys and 0.4493 between the 2018–19 LiDAR and the 2009 multibeam.

Neighboring cells sample the same terrain, so the correlation coefficients describe agreement between maps and the cell counts are not independent sample sizes. Local point timestamps for the 2018–19 product fall on November 25, 2018. The modern geometry persisted across the storm at survey resolution. These comparisons do not constrain how it formed.

The earlier record is less uniform. The 1934–35 survey H05727 has 79 valid soundings within 325 m of the study point. After fitting a survey-specific plane, the 5th-to-95th percentile span of these soundings is 0.65 m. At the same locations the modern surface spans 1.67 m, and the two records correlate at 0.09. Several modern western ridges cross areas where the historical soundings are relatively level. The relief may have formed or grown after 1935. H05727 may also have under-resolved existing relief, because it used mean low water, recorded depth in whole feet and missed the summit. One digitized value of 10 ft conflicts with the 19 ft figure on the original smooth sheet.

The 1997 survey H10748 agrees closely with the modern surface. At 47 matched points the spans are 2.13 m in 1997 and 1.79 m today, with a correlation of 0.95, so the modern relief was broadly present by 1997. These data constrain change between surveys but do not date individual ridges. The 1928 survey H04801 has no coverage at the site.

Dumping in the area is documented. The September 1935 review, page 3 (PDF page 20), records earlier dumping south of the channel without locating individual loads. The dumping-ground polygon on the NOAA chart covers 86.2% of a 325 m-radius disk centered on the published study point (25.749808°N, 80.122717°W), and Florida's Unified Reef Map classifies

73.5% of the same disk as artificial habitat. Walker (2009, p. 9) interpreted probable dredge spoil over natural hardbottom in this area. Neither map locates individual loads, and a habitat class does not date the substrate. The construction history at the site remains unresolved.

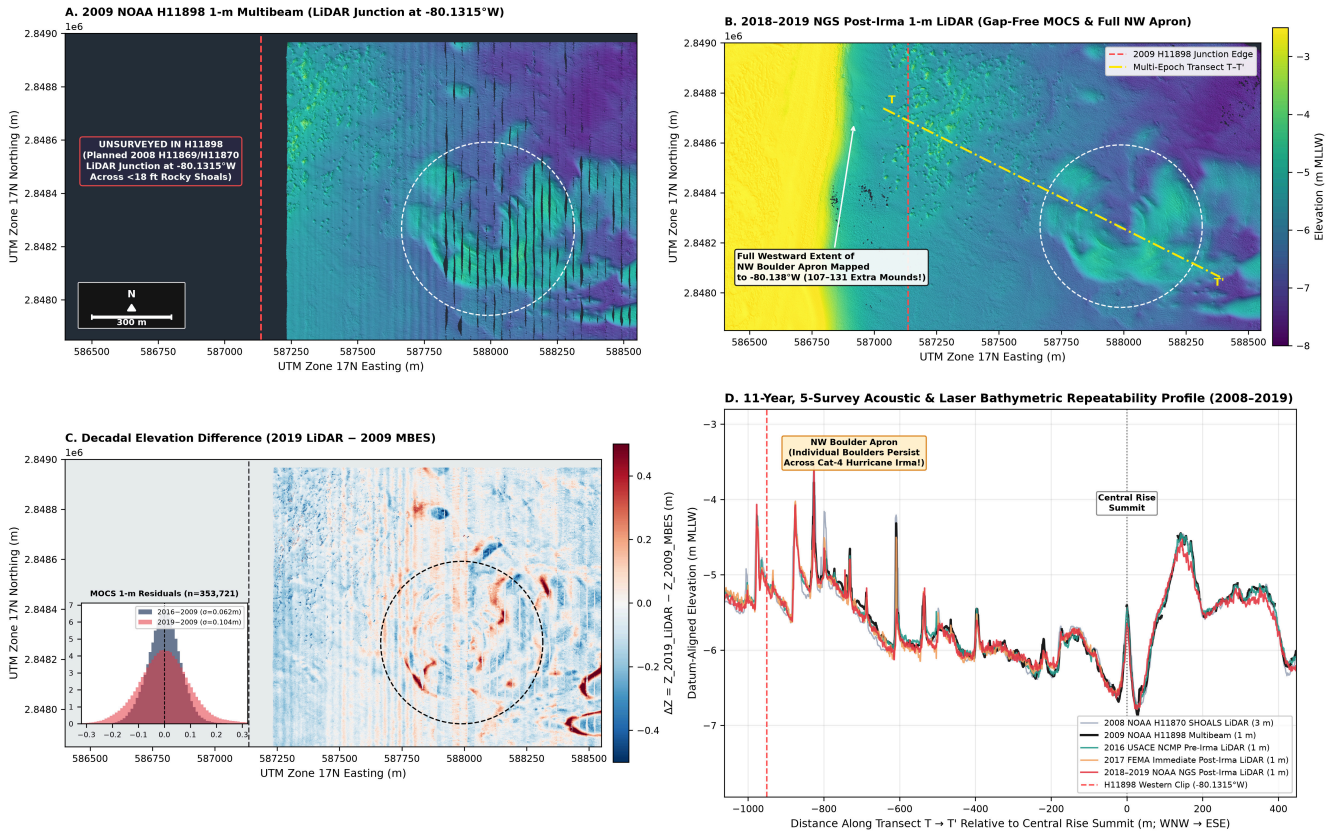

Figure 3. Multi-epoch, cross-sensor comparison of MOCS and westward extension of mapping across the NW Boulder Apron (H11898-28) before and after Hurricane Irma (September 2017). **(A)** 2009 NOAA H11898 1-m acoustic multibeam, showing the planned survey junction at -80.1315°W (80°07'53"W) with the 2008 airborne LiDAR surveys H11869/H11870. **(B)** 2018–2019 NOAA NGS post-Irma 1-m green-laser (532 nm) topobathymetric LiDAR, which provides continuous coverage west of -80.1315°W. West of the junction, 107 additional submerged mounds are detected in the 2018–2019 survey and 131 in the 2016 survey (776 and 911 mounds in total, respectively). The westernmost mounds reach -80.1384°W, 1.65 km WNW of MOCS. **(C)** Cell-by-cell difference map (2018–19 LiDAR – 2009 multibeam) and residual histogram (n = 353,721). σ_ΔZ relative to the 2009 multibeam is 0.062 m for the 2016 survey and 0.104 m for the 2018–2019 survey. **(D)** Five-epoch transect T→T' (2008–2019) showing decimeter-scale agreement of the Central Rise, the rings, and individual meter-scale NW mounds before and after Hurricane Irma.

4.2 Northwest boulder apron (H11898-28) compared with split-scow barge spoil (H11898-2/3)

In H11898, the straight north–south cutoff along -80.13148°W (80°07'53"W) is the planned survey junction with the 2008 airborne LiDAR surveys H11869 and H11870. The junction was placed across rocky shoals shallower than 18 ft (5.5 m), which were unsafe for R/V *Able II* (Reynolds, 2009, pp. 10, 151). It does not mark the edge of the boulder field.

East of that line, 0.5-m multibeam (H11898_Rky_Area_North) and 200% Klein 3000 side-scan sonar mapped H11898-28. There, rock blocks shoal to 2.77–2.92 m MLLW (9.09–9.60 ft) and were reported as Danger-to-Navigation Items #3–#12. NOAA Electronic Navigational Chart US5FL22M encodes them with the seabed attributes NATSUR = "Coral" and NATQUA = "Calcareous" (Reynolds, 2009, pp. 27–28, 159).

The 1-m bathymetric LiDAR extends the mapping west across -80.13148°W. The 2019 NGS survey detects 776 discrete mounds, interpreted as boulders or rock blocks. Of these, 669 lie east and 107 lie west of the junction, so 13.8% are west of it. The westernmost reaches -80.13839°W, 1,649 m WNW of MOCS. The 2016 USACE survey detects 911 mounds, with

780 east and 131 west (14.4% west), extending to -80.13584°W, 1,450 m WNW (**Figure 3B**, **Figure 4A**). Pre- and post-Irma Fine-BPI across the apron correlate at r = 0.897–0.915, and at r = 0.926 across the 550 × 500 m core window in Figure 4D. This shows repeatable relief at survey resolution. The movement of individual blocks was not tracked.

Structure-tensor anisotropy (**Figure 4C, E, F**) distinguishes the NW Boulder Apron (H11898-28) from the documented hopper and split-scow barge spoil in H11898-2/3, 2.4–2.6 km ENE. H11898-2 contains 15–20 parallel, straight east–west ridges that follow scow tracks. Its dominant strike is 87.6°, orientation coherency is 0.631, the 90th-percentile slope is 20.26°, and the 95th-percentile roughness over 5 × 5 m windows is 60.7 cm. H11898-28 consists of equant, non-collinear clusters with coherency of 0.217–0.236 and 90th-percentile slopes of 5.69°–8.28°. It shows no scow-track periodicity. This contrast shows that the apron lacks the track pattern of the H11898-2/3 spoil. It does not exclude placement by other dumping methods, and it does not establish the source of the blocks.

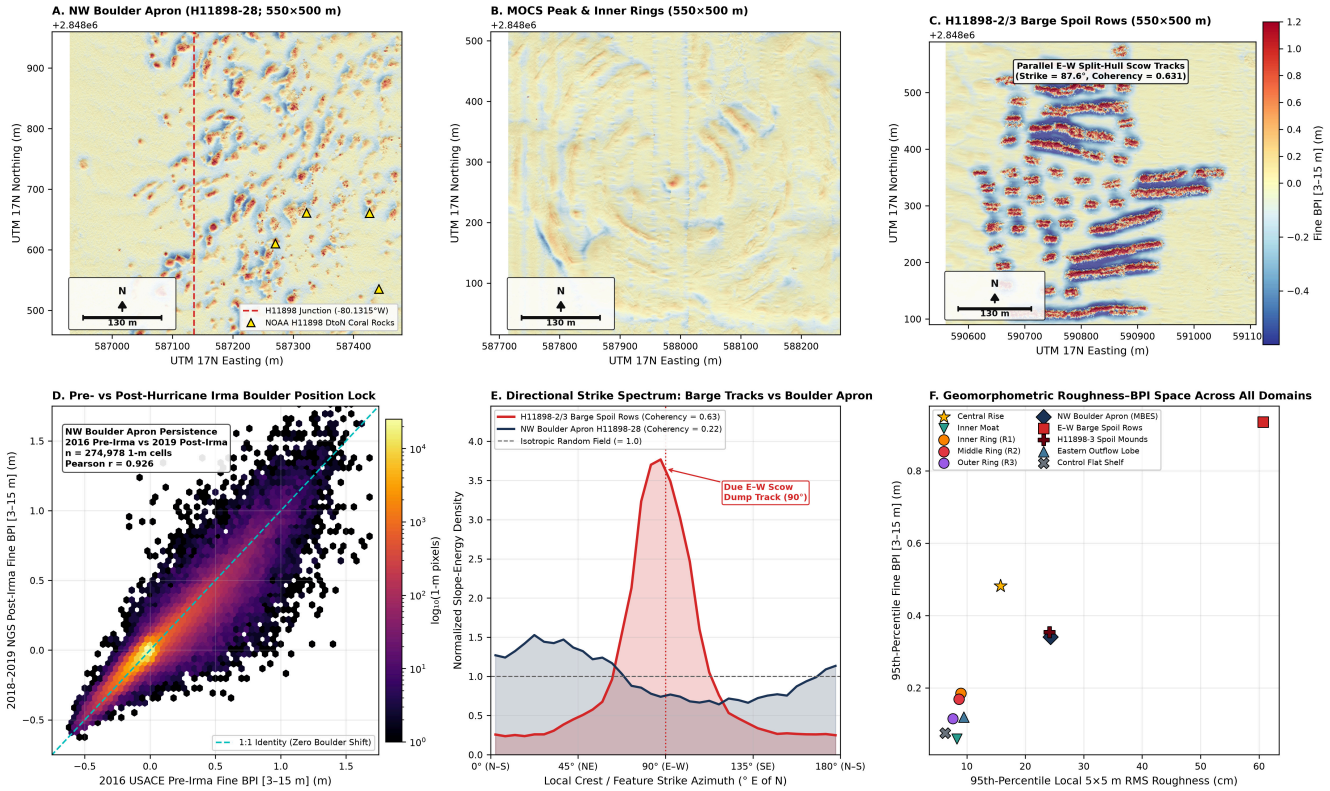

Figure 4. Texture, pre- and post-storm repeatability, and directional anisotropy of the NW Boulder Apron (H11898-28) compared with documented split-hull barge spoil (H11898-2/3). **(A–C)** Equal-scale (550 × 500 m) Fine-BPI (3–15 m) maps of **(A)** the NW Boulder Apron straddling the -80.1315°W H11898 junction (yellow triangles: NOAA H11898 coral-rock danger-to-navigation items), **(B)** the MOCS Central Rise and inner rings, and **(C)** the parallel E–W split-hull scow dump rows of H11898-2/3 (strike = 87.6°, coherency = 0.631). **(D)** Cell-level scatter density of 2016 pre-Irma versus 2018–2019 post-Irma Fine-BPI across the NW Boulder Apron (n = 274,978, r = 0.926), showing repeatable mapped roughness. **(E)** Normalized directional strike spectrum. The scow dump rows show a sharp E–W peak at 90° (coherency = 0.63), and the NW Boulder Apron is near-isotropic (coherency = 0.22). **(F)** Separation of nine domains in the space of 95th-percentile roughness versus Fine-BPI.

5. Marine geophysics, sub-bottom acoustics, vibracores, dredging history and 3D magnetic modeling

5.1 Georeferencing of Aley (2021) tracklines, picks M01–M33 and hardbottom exclusion

The native ArcGIS rasters in Aley (2021, Slides 11–12) were registered by affine transformation to the official BOEM Marine Minerals Information System (MMIS/GeoSeas) polylines for USACE_M20PG00014_StateWaters (BOEM, 2024). This BOEM record contains 39 Miami-Dade reconnaissance tracklines. Its DataTypes field reads verbatim: "Sub-Bottom

Seismic, Multi-Beam Bathymetry, Magnetometer, Side Scan Sonar". The root-mean-square (RMS) residual is 2.56 m (8.39 USft) on the main panel (Im2) and 0.59 m (1.94 USft) on the northeastern borrow inset (Im3) (Figure 5). Within these residuals, the registered maps support three spatial observations.

1. No geophysical or core coverage in the NW Boulder Apron (H11898-28). Under Florida Department of Environmental Protection (FDEP) Rule 62B-41, Taylor Engineering mapped and excluded all colonized hardbottom west of -80.12406°W and north of 25.7500°N (Aley, 2021, Slide 5). This area lies outside the surveyable sand polygon DA01-R077. On the registered slides, no tracklines, magnetometer picks or vibracores fall inside the apron, so the 2020 survey provides no direct observation of its composition. One west–east line, Line 37, crosses the western rim of MOCS, Ring R1, the Central Peak and the eastern rings. One north–south line, Line 36, grazes eastern Ring R1.
2. Inventory and setting of the 33 magnetometer picks (M01–M33). At high magnification the slides resolve 33 individual cyan diamond symbols, 27 in Im2 and 6 in Im3, which merge into about 27–28 clusters at slide scale. The symbols give locations only, without amplitudes or material identification.

No picks occur on the Central Peak. Five clusters (6 symbols) coincide with the concentric rings of MOCS. M01 lies at 269.0 m W on the western outer ring, M02 at 162.6 m W on western Ring R1, and M04 at 214.4 m NNE on the northeastern outer ring. The cross-line pair M05+M06 lies at 68.4–81.5 m E on eastern Ring R1 and was detected independently on Line 37 and Line 36. M07 lies at 243.9 m E on the eastern outer ring. The slides do not identify the sources of these ring-coincident picks.

Twenty picks lie inside the Eastern Outflow Lobe and Spoil Area. They include M26, directly atop the Line 42 dredge-spoil mound, and M16–M20, a 125.4 m linear string of five picks on Line 34 whose shape is consistent with steel dredge pipe or wire rope, although the source is inferred. M27 lies about 45 m north of the 120-in sewer outfall pipeline. Six picks (M28–M33) lie in the distal NE borrow area (Figure 5).

Taylor Engineering (2021), Appendix F, identifies the instruments as a Geometrics G-882 digital cesium magnetometer and an EdgeTech SB-512i sub-bottom profiler and reports a final countywide tally of 51.7 line-miles and 59 cores. The local slides cover a subset of that survey.

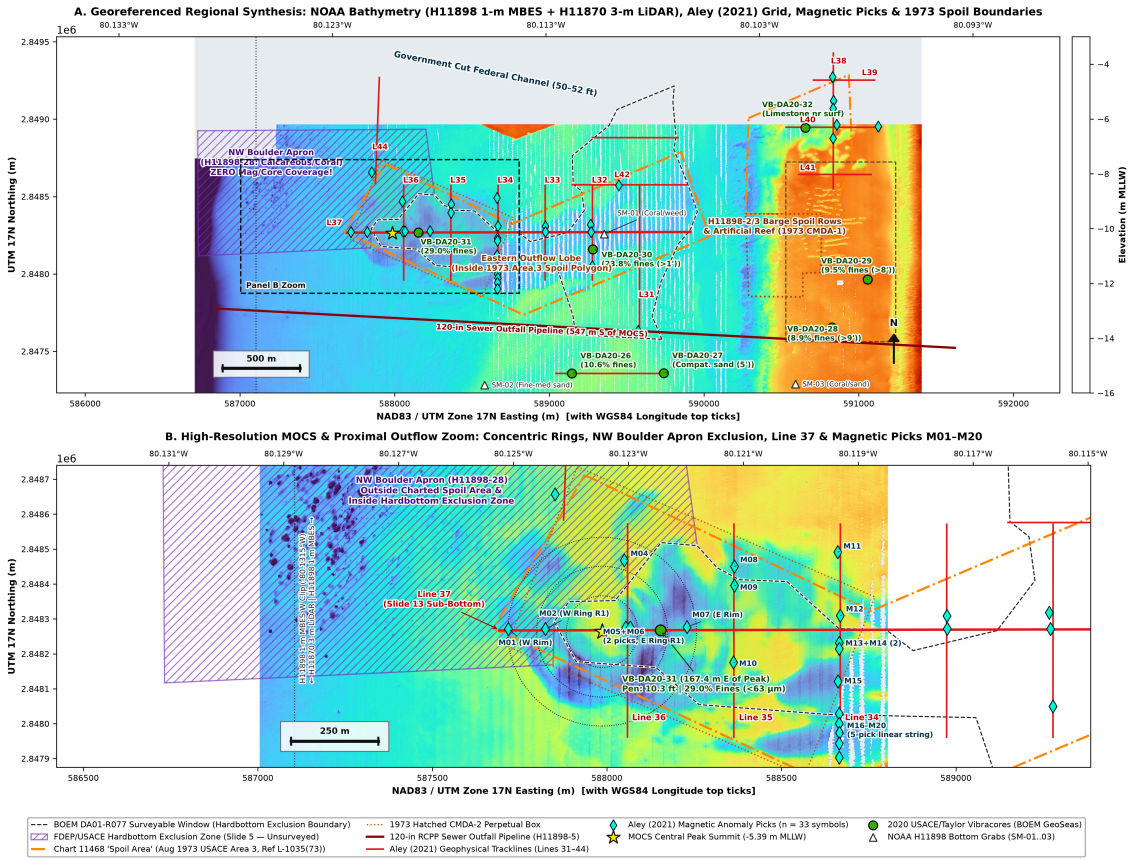

Figure 5. Georeferenced synthesis of the 2020 USACE/Taylor geophysical and vibracore survey (Aley, 2021; USACE_M20PG00014_StateWaters, RMS = 0.59–2.56 m), the 1973 USACE Spoil Area boundaries (Ref L-1035(73)) and 2008–2009 NOAA multibeam and LiDAR bathymetry. **(A)** Regional trackline grid (Lines 31–44), all 33 cyan magnetometer anomaly symbols (M01–M33), VB-DA20 vibracores, H11898 grab samples (SM-01..03) and the purple hatched FDEP/USACE hardbottom exclusion zone. The exclusion zone covers H11898-28, which has no magnetometer or core coverage. **(B)** Zoom over MOCS and the proximal Eastern Outflow Lobe. Line 37 crosses the Central Peak (0 picks) and the concentric rings (M01, M02, M04, M05+M06, M07). Vibracore VB-DA20-31 lies 167.4 m E and contains 29.0% fines. The Spoil Area of Chart 11468 (1973 Area 3, orange dash-dot) overlaps the MOCS rings and the Eastern Outflow Lobe. The NW Boulder Apron (H11898-28) lies outside it to the west.

5.2 Shallow reflector on sub-bottom Line 37 and loose-spoil control on Line 42

Aley (2021) Slide 13 shows the SonarWiz Channel 1 high-frequency sub-bottom profile for Line 37 (25°44.9866'N). The line passes about 3–10 m north of the -5.387 m apex of the 2D peak. The slide carries its own caution about structure below bedrock: *"Seismic images collected are inconclusive / High Frequency = Low Penetration"*.

The digitized 2020 Line 37 seabed reflection was cross-correlated with the 2009 H11898 1-m multibeam profile. The best fit gives a towfish depth of z_fish = 3.46 m (11.34 ft) below MLLW and an eastward tow-cable layback of +12.95 m (+42.5 USft). With these corrections, the 2009-to-2020 seabed correlation rises from r = 0.7909 to r = 0.9591 (RMS = 0.155 m) (Table 5, Figure 6A–B). The fitted shift describes the best alignment to the NOAA profile. It is not an independent navigation measurement. The close agreement indicates that the seabed profile along this line persisted between the two surveys. It does not show how the relief formed.

The red R1 contact is visible on the flanks and stops across the central rise. An earlier version of Figure 6B placed the missing contact 0.08 m below the mapped seafloor at the center and introduced a pocket in the eastern moat. Those segments were drawn without supporting picks. The revised figure leaves the central gap open. The data do not measure cover thickness beneath the summit. They also do not show whether bedrock is rooted there.

The bottom-left panel on Slide 14 shows line D42W. The right panel shows D41W. On Line 42, a shallow, approximately level return lies beneath a mound in the mapped spoil area. Its geometry differs from the interpreted flank picks on Line 37. Notes accompanying the slides describe shallow penetration of roughly 5–10 ft and identify deeper apparent layers as multiples. The shallow contact could include rock or gravel. The contrast between the two lines is consistent with a difference in construction between the spoil mound and the ring flanks. Two profiles are too few to establish that difference. They cannot resolve how the central rings are built, and they do not rule out redeposited carbonate over hardbottom.

Table 5. Sub-bottom acoustic stratigraphy across MOCS (Line 37, Slide 13), registered to the 2009 multibeam profile, with the northern Spoil Area mound (Line 42, Slide 14 bottom-left) as a control. Reflector elevations are interpreted from the conference panels, and thicknesses are given for two assumed sound speeds. Reflector gaps beneath the central rise and the eastern moat prevent a measured thickness there.

Acoustic / Structural Zone	Trackline & EPSG:2236 X Range (USft)	Seafloor Elev. (m MLLW)	Sediment Thickness (c = 1,500 m/s)	Sediment Thickness (c_{sed} = 1,650 m/s)	Sub-Bottom Reflector R1 Geometry & Interpretation
Western Ring R1	L37: 944,410–944,660	-5.22 to -5.97	1.33 m mean (1.89 max)	1.47 m mean (2.08 max)	Elevated flank pick on Reflector R1 (+0.6–0.9 m above moat)
Western Annular Moat	L37: 944,730–944,890	-6.07 to -6.70	1.47 m mean (1.81 max)	**1.62 m mean (1.99 max)**	Concave acoustic contact (-8.1 to -8.5 m MLLW), interpreted as ponded fill
MOCS Central Peak	L37: 944,890–945,010	-5.54 MBES (-5.39 apex)	Unresolved	Unresolved	R1 is unpicked across the central rise.
Eastern Inner Moat	L37: 945,010–945,085	-6.82 MBES (-7.04 CHIRP)	Unresolved in the gap	Unresolved in the gap	Seafloor forms a narrow depression in the comparison profile.
Eastern Ring R1	L37: 945,110–945,320	-5.22 to -5.97	1.33 m mean (1.98 max)	1.46 m mean (2.17 max)	Interpreted shallow contact under ridge (Reflector R1 at -6.5 m; M05+M06)
Line 42 Spoil Control	L42: 949,500–950,200	-6.68 crest (1.74 m mound)	2.39 m under crest	**2.63 m under crest**	Mapped mound at M26 above a shallow, nearly flat acoustic contact.

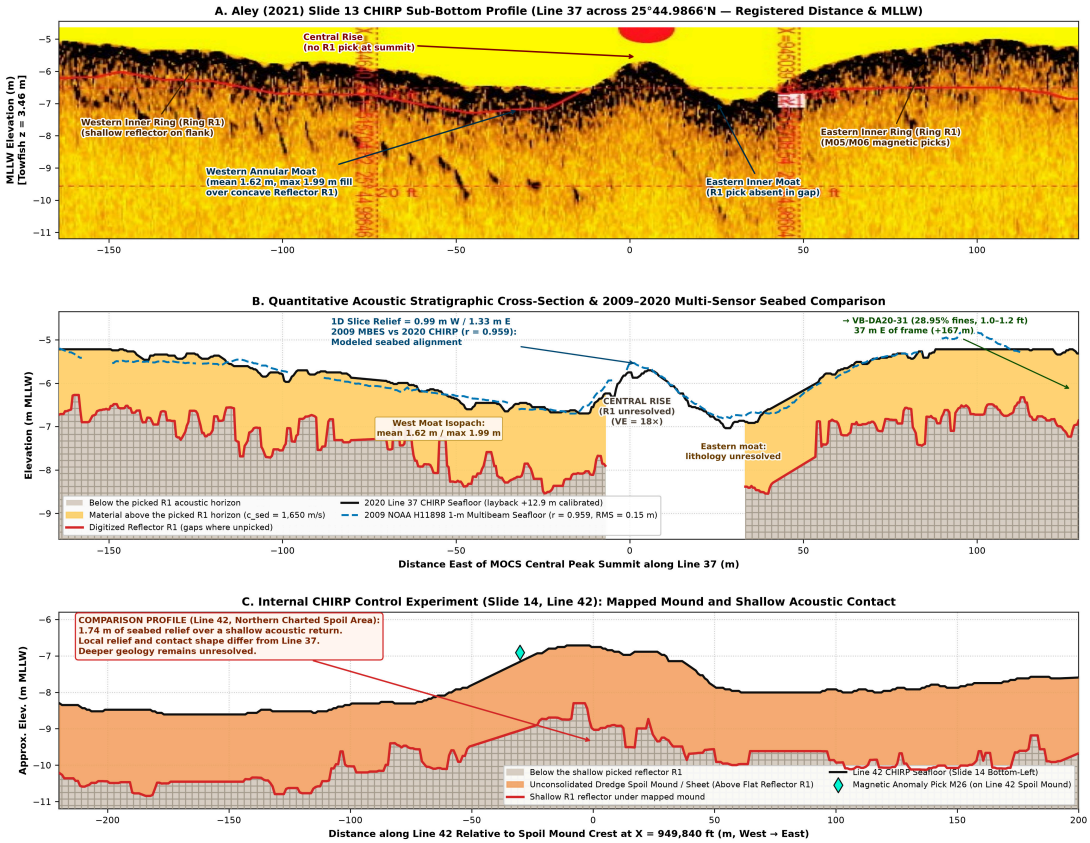

Figure 6. Panel A shows the published Line 37 profile. Panel B compares its registered seabed trace with 2009 multibeam bathymetry. The red line follows the flank segments of the published reflector interpretation. Its central gap is retained. The darker shading below the pick does not indicate lithology or deep structure. Panel C shows the Line 42 comparison across a mound in the charted spoil area. Elevations depend on the towfish registration and an assumed sound speed. Aley (2021) described the profiles as inconclusive.

5.3 Dredge-disposal history (1905–2015) and BOEM vibracore sedimentology (VB-DA20)

The archival blueprint on Aley Slide 9 was georeferenced to Chart 11468 with an RMS error of 1.93 m. The sheet is Ref L-1035(73) / Bp 84508-16, the USACE Jacksonville District 36/38-ft Miami Harbor deepening plan authorized under Public Law 90-483. It was compiled onto Coast & Geodetic Survey Chart 547 (NOAA Chart 11468) on August 24, 1973, with the annotation 8/24/73 JWS (USACE, 1973) (Figure 7C). Together with hydrographic records from 1919–2015 (Duane & Meisburger, 1969; USC&GS, 1919, 1935; USEPA, 1995; USACE, 2004; Reynolds, 2009), the blueprint shows two spatial relationships that bear on the origin question in different ways.

1. Charted Area 3 (H11898-1) overlaps the MOCS rings and the Eastern Outflow Lobe. The August 1973 Area 3 polygon (Chart 11468 Spoil Area / H11898-1) contains the hatched CMDA-2 Perpetual area and has a western vertex at -80.125798°W. It encloses the entire Eastern Outflow Lobe and overlaps the concentric rings of MOCS (-80.1227°W). The 1935 H-5727 Review (p. 3) also records open-water dumping south of the Entrance Channel before 1935 (USC&GS, 1935). During the H11898 survey, Ocean Surveys, Inc. first placed the 13.72 ft (4.20 m) least depth of H11898-1 on the SE ring crest of MOCS (25°44'55.67"N, 80°07'17.21"W), 163.6 m SE of the summit. NOAA Atlantic Hydrographic Branch reviewers later moved the least depth 1.52 km ENE to 25°45'11.169"N, 80°06'28.709"W (Reynolds, 2009, p. 21). Rock from the later 42/44-ft deepening (1990s–2005) and the 50/52-ft PortMiami Deep Dredge (2013–2015) was reportedly taken 4.7 nmi offshore to the deepwater Miami Ocean Dredged Material Disposal Site, at 102–235 m depth (USEPA, 1995; USACE, 2004). The 2013–2015 project postdates the 2009 image. Earlier harbor works do not. Regional dumping near MOCS is therefore documented. The positions of individual loads and the construction history of the disposal area remain unresolved.

2. The NW Boulder Apron (H11898-28) lies outside Area 3, and nearby shoals predate modern deepening. H11898-28 spans -80.126°W to -80.138°W, entirely west of the 1973 Area 3 Spoil Area, described as *"north of the sewer pipeline and west of the spoil area"* (Reynolds, 2009, p. 159). Rocky shoals of 10–12 ft south of the South Jetty were already charted on 1919 H-4075, before modern harbor deepening (USC&GS, 1919). The apron therefore lies outside the mapped 1973 disposal polygon, and some nearshore rock relief existed by 1919, although these records do not establish how that relief formed. Because pre-1935 dumping south of the Entrance Channel is documented, the charts alone cannot exclude unmapped disposal outside Area 3.

Table 6 summarizes the 2020 BOEM GeoSeas vibracores (core_samples.json, NAVD88; BOEM, 2024). Core VB-DA20-31 lies 167.4 m east of the MOCS summit at -19.0 ft NAVD88. It penetrated 10.3 ft and recovered 8.5 ft (83%). Fines are 28.95% at 1.0–1.2 ft and 7.89% at 3.0–3.2 ft (Taylor Engineering, 2021, Appendix D). Core VB-DA20-30 lies 1,300.4 m east, in the Eastern Outflow Lobe, at -21.1 ft NAVD88. It penetrated 19.7 ft and recovered 17.1 ft (87%), and no bedrock was recovered in the logged run. A selected interval has reported fines of 23.8% (Figure 7A–B). Core VB-DA20-32, 2,755.5 m ENE, reached refusal. The material at refusal is not verified in these records.

For comparison, five ESE–SE shelf and reef-gap cores (VB-DA20-23, -25, -26, -28, -29), 1.47–3.61 km from the summit, contain 8.9%–14.0% fines. The open-shelf core VB-DA20-24 (2,378.6 m SE, -28.1 ft NAVD88) contains 22.3% fines. Elevated fines near MOCS are therefore not unique on this shelf. The values also come from selected intervals, and in VB-DA20-31 the fines decrease with depth.

The unconsolidated carbonate silt in VB-DA20-31 and VB-DA20-30 is compatible with several sources. Natural candidates include rock flour from impact resurge in shallow water and marl associated with paleokarst. Anthropogenic candidates include silt settling from the harbor ebb plume during cutterhead dredging and reworked pre-1975 fine spoil within Area 3. The existing core records do not discriminate among these sources. A proposed Stage-3 program, not yet approved or carried out, would address them with ^{210}Pb, ^{137}Cs and ^{14}C dating and with scanning electron microscopy (SEM) of grain angularity. Excess ^{210}Pb or measurable ^{137}Cs throughout the silty unit would favor recent deposition, such as dredge plume fallout or spoil. Older ^{14}C ages with no modern radionuclide signal would favor a natural source. Angular grains alone would not separate impact comminution from mechanical dredging, so SEM results would need to be read together with the dating.

Table 6. 2020 USACE and Taylor Engineering VB-DA20 vibracore records around MOCS and on the Miami-Dade shelf (BOEM GeoSeas, USACE_M20PG00014_StateWaters, countywide coring June 23–July 1, 2020). Vertical datum is NAVD88.

Vibracore ID	WGS84 (Lat °N, Lon °W)	Geodesic Dist. & Azimuth from Summit	Seabed Elev. (ft NAVD88)	Pen. / Rec. (ft, %)	<63 µm Fines & BOEM GeoSeas Lithologic Summary (with author annotations)
VB-DA20-31	25.749775, -80.121025	**167.4 m E (089.1°)** — MOCS E margin	-19.0	10.3 / 8.5 (83%)	28.95% at 1.0–1.2 ft; 7.89% at 3.0–3.2 ft — Sand flat and mounds (Line 37)
VB-DA20-30	25.748731, -80.109781	**1,300.4 m E (095.0°)** — E Outflow Lobe	-21.1	19.7 / 17.1 (87%)	**23.8% fines below 1'** — No rock hit (Slide 15 0–10 ft trays)
VB-DA20-32	25.755739, -80.096036	2,755.5 m ENE (076.1°) — NE DA3-R074	-27.8	20.0 / 17.0 (85%)	**Limestone encountered near surface** (% fines not reported)
VB-DA20-24	25.732876, -80.108035	**2,378.6 m SE (141.8°)** — Open shelf	-28.1	13.2 / 10.7 (81%)	**22.3% fines** — Open inner-shelf mud pocket *(off-structure comparison)*
VB-DA20-26	25.741493, -80.111196	1,472.3 m SE (128.4°) — S sand flat	-30.5	13.4 / 11.1 (83%)	**10.6% fines** below 1' (Line 30, S of sewer outfall)
VB-DA20-28, -29	25.7441–.7469, -80.0944–.0921	2,907–3,086 m ESE–E — Inter-reef trough	-46.1, -47.7	18.0–20.0 (80–88%)	**8.9% & 9.5% fines** below 8'–9' (≤10% clean sand 0–8')
VB-DA20-25, -23	25.7361–.7305, -80.0935–.0937	3,294–3,608 m ESE–SE — 3rd Reef gaps	-55.4, -51.2	20.0 / 17.8 (89%)	**11.2% & 14.0% fines** (0.25 mm mean grain size in -23)
VB-DA20-27, -33..35	25.7415–.7679, -80.1053–.1192	1,973–2,235 m ESE & N–NE of Cut	-18.9 to -30.0	10.1–15.8 (70–92%)	Compatible sand (≤10% fines) in -27, -33, -35; 35.8% gravel in -34

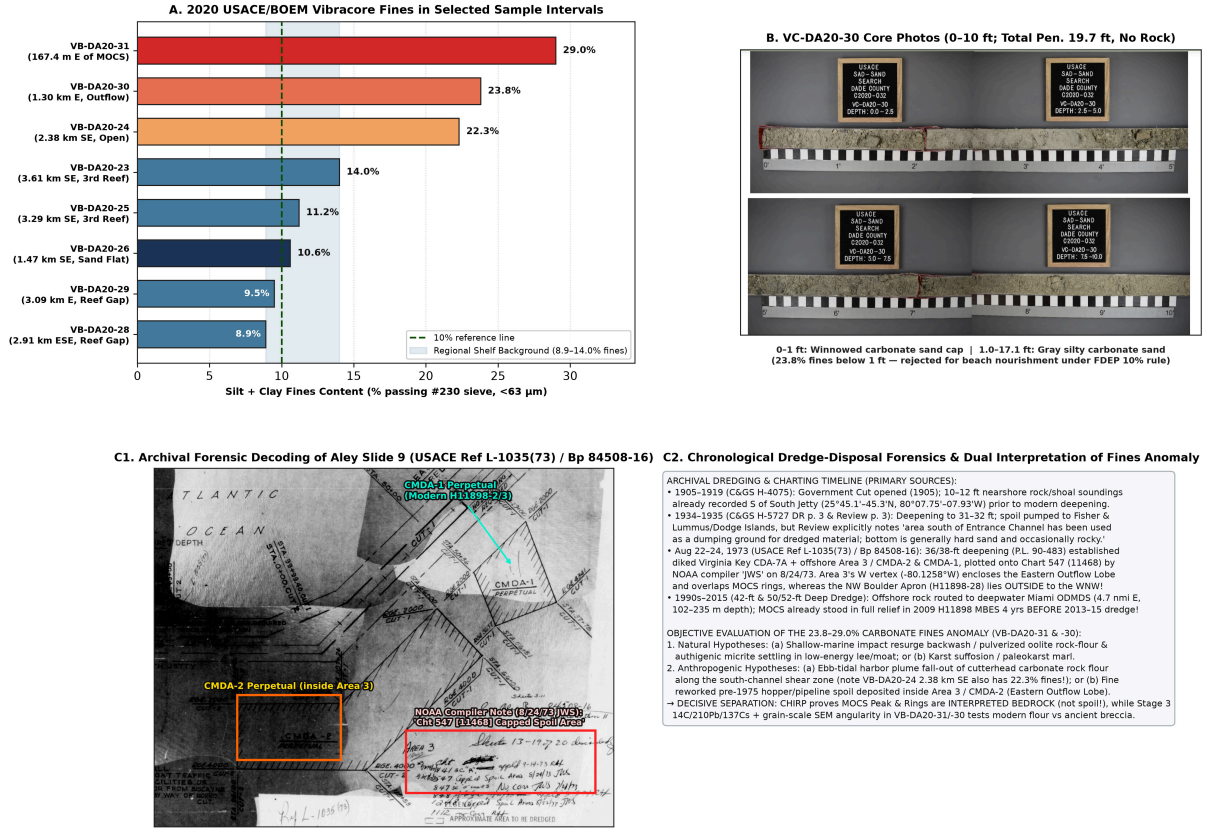

Figure 7. Vibracore sedimentology (USACE_M20PG00014_StateWaters) and archival records of Government Cut dredging and disposal (1905–2015). **(A)** Fines in selected sample intervals, ranked. Values vary with depth. The plot uses rounded values from the published presentation. It compares VB-DA20-31 (29.0%) and VB-DA20-30 (23.8%) with the 8.9%–14.0% ESE–SE shelf background (n = 5) and with open-shelf core VB-DA20-24 (22.3%). **(B)** Core photographs of VC-DA20-30 (0–10 ft split runs; Aley, 2021, Slide 15). Clean, winnowed carbonate sand at 0–1 ft overlies homogeneous olive-gray, matrix-supported silty carbonate sand at 1.0–17.1 ft. **(C1–C2)** Georeferenced August 24, 1973 USACE Harbor Deepening blueprint (Ref L-1035(73) / Bp 84508-16; Aley Slide 9) showing Area 3 (CMDA-2 Perpetual) and CMDA-1 Perpetual (H11898-2/3), with a chronology of dredging and disposal.

5.4 3D vector magnetostatic modeling and stage-2 gradiometric discrimination

At MOCS (B_0 = 43,550 nT, inclination I = +54.5°, declination D = −6.7°), the peak-to-peak scalar total-field anomaly of a dipole source is defined as $\Delta T_{pp} \equiv \max(\|\mathbf{B}_0 + \Delta\mathbf{B}\| - B_0) - \min(\|\mathbf{B}_0 + \Delta\mathbf{B}\| - B_0)$. The vertical sensor-to-source separation is $R = h_{sensor} + d_{burial}$. The exact dipole expression is (Breiner, 1973; Blakely, 1995):

$$\Delta T_{pp}(R) = K_{pp}(I)\frac{m}{R^3} = K_{pp}(I)\frac{\sigma_{eff} M_{src}}{R^3}, \qquad K_{pp}(54.5°) = 185.847\ \text{nT m}^3\ (\text{A m}^2)^{-1} \tag{2}$$

The forward models use effective mass magnetizations σ_{eff} calibrated for meteorites and ferrous alloys (Terho et al., 1993; Pilkington & Grieve, 1992; Rochette et al., 2003, 2008). Under the assumed magnetizations and pick thresholds, the 3D results (Table 7, Figure 8) give three constraints on modeled sources.

First, shocked pure Miami Limestone oolite is too weakly magnetized to produce a mapped pick. Modeled as a 30 m × 2 m central-peak disk at h = 3.5 m, with <500 ppm Fe, $\chi = 10^{-4}$ SI and a Koenigsberger ratio Q = 1.5, it yields 1.42 nT peak-to-peak, below the 2–5 nT thresholds assumed here. This may explain why no pick was mapped at the central rise on Line 37. It also means that a scalar survey of this kind can neither detect nor exclude a shocked carbonate target by itself.

Second, a 5 nT pick on the MOCS rings at R = 3.0–5.0 m requires 0.9–4.2 kg of stray port steel (σ_{eff} = 0.80 A m^2 kg^{-1}), 4.8–22.4 kg of partially preserved Fe–Ni meteorite (σ_{eff} = 0.15 A m^2 kg^{-1}), or 29.1–134.5 kg of oxidized meteoritic iron shale (σ_{eff} = 0.025 A m^2 kg^{-1}). A thermally roasted *terra rossa* paleosol lens also exceeds the threshold, at 5.71 nT (Perkins, 1977). Steel reaches the threshold with far less mass than either meteoritic source. A ring pick is therefore consistent with harbor debris, meteoritic material or altered paleosol, and any source assignment remains an inference.

Third, scalar amplitude scales as m/R^3 and vertical gradient as $\partial(\Delta T)/\partial z \propto m/R^4$, so sources at different depths can give the same scalar anomaly with different gradients. In the model, a 3.1 kg seabed steel cable at R = 3.5 m and an 83.3 kg buried Fe–Ni fragment at R = 6.0 m both produce a 10.7 nT scalar anomaly. A vertical gradiometer with a 1.0 m baseline would separate them, because their gradients differ by +43% (5.98 vs. 4.19 nT/m) and their full widths at half maximum (FWHM) are 3.6 m and 6.2 m, respectively (Figure 8C). This Stage-2 gradiometric survey is proposed and has not been carried out.

Table 7. Modeled 3D vector magnetostatic mass thresholds (2 nT, 5 nT, 20 nT) and extended-body anomalies at MOCS (B_0 = 43,550 nT, I = +54.5°, D = −6.7°).

Candidate Magnetic Source Class	Magnetization / Susceptibility	Separation R (m)	Min. Mass for 2 nT	Min. Mass for 5 nT	Min. Mass for 20 nT
Stray Ferrous Port / Dredge Steel (ρ = 7,850 kg m^{-3})	σ_{eff} = 0.80 A m^2 kg^{-1}	3.0 / 5.0 / 8.0	0.4 / 1.7 / 6.9 kg	**0.9 / 4.2 / 17.2 kg**	3.6 / 16.8 / 68.9 kg
Partially Preserved Fe–Ni Meteorite (ρ = 7,500 kg m^{-3})	σ_{eff} = 0.15 A m^2 kg^{-1}	3.0 / 5.0 / 8.0	1.9 / 9.0 / 36.7 kg	**4.8 / 22.4 / 91.8 kg**	19.4 / 89.7 / 367.3 kg
Oxidized Meteorite "Shale" (ρ = 4,200 kg m^{-3})	σ_{eff} = 0.025 A m^2 kg^{-1}	3.0 / 5.0 / 8.0	11.6 / 53.8 / 220.4 kg	**29.1 / 134.5 / 551.0 kg**	116.2 / 538.1 / 2,204 kg
Shocked Pure Miami Oolite Disk (30 m × 2.0 m)	$\chi = 10^{-4}$ SI, Q = 1.5	h = 3.5 (d_b = 0)	—	**1.42 nT peak-to-peak**	Sub-threshold *(0 peak picks)*
Roasted *Terra Rossa* Paleosol (20 m × 0.5 m)	$\chi = 10^{-3}$ SI, Q = 2.5	h = 3.5 (d_b = 0)	—	**5.71 nT peak-to-peak**	Broad ~20 m edge dipole
Disseminated Meteoritic Oxide Lens (10 m × 0.5 m)	χ = 0.015 SI, Q = 1.0	R_{top} = 4.5	—	**27.14 nT peak-to-peak**	Strong mappable lens anomaly (modeled)

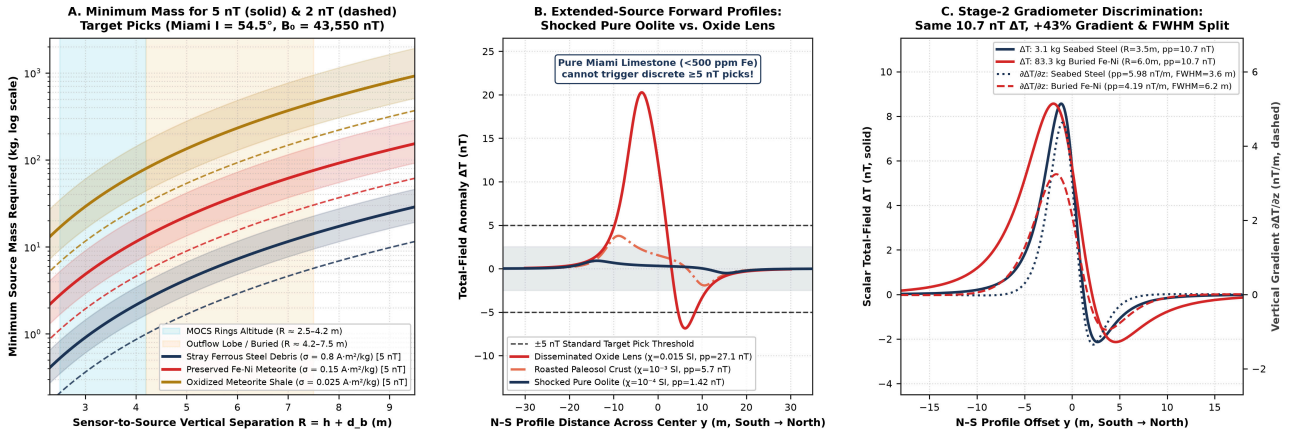

Figure 8. Three-dimensional vector magnetostatic forward modeling (B_0 = 43,550 nT, I = +54.5°, D = −6.7°) and proposed Stage-2 gradiometric source discrimination. **(A)** Minimum source mass for 5 nT (solid) and 2 nT (dashed) target picks across R = 2.3–9.5 m, for stray steel, preserved Fe–Ni meteorite and oxidized meteorite shale. **(B)** North–south total-field profiles across extended 3D disks. Pure shocked Miami Limestone (1.42 nT) falls below the ±5 nT pick criteria. A 0.3 vol% disseminated oxide lens yields 27.1 nT (+20.28 / -6.87 nT). **(C)** Two sources with the same 10.7 nT scalar anomaly: 3.1 kg of seabed steel at R = 3.5 m and 83.3 kg of buried Fe–Ni at R = 6.0 m. A 1.0 m vertical gradiometer separates them by gradient (5.98 vs. 4.19 nT/m, +43% split) and by FWHM (3.6 vs. 6.2 m).

6. Reassessment of the 2020 dive and bathymetry comparison

Paris, Robertson and Schwartz (2020) report specimens from thirty sampling locations, including the central area, the ridges and the northwest boulder field. They describe the material as oolitic limestone and interpret the pattern as uneven dissolution. Their surface observations constrain what the sampled material is. The comparisons below use their published maps and depth reports.

1. **Scope of the published analyses.** The paper gives June 27, 2020 as the dive date and July 11 as the acceptance date. The text describes surface inspection and shows a low-power microscopic image. It does not report polished thin sections, systematic shock-petrographic examination, electron backscatter diffraction (EBSD) or geochemical tests. The dates do not show how the authors or reviewers divided their work across that interval.
2. **Shock-pressure expectations and surface sampling.** The Paris hand-sample report relies mainly on macroscopic inspection of 30 specimens collected from several parts of the structure. The team reports ooids, calcite and quartz sand and illustrates one northwest-ring sample microscopically. The paper gives no modal mineral percentages for the 30 specimens. Macroscopic inspection can detect shatter cones but cannot resolve quartz planar deformation features (PDFs), which require microscopy. More informative tests would concentrate any acid-insoluble quartz with 10% HCl for PDF searches (French & Koeberl, 2010) and would examine calcite twins at sub-optical resolution. Bioeroded surface chips from the outer slump rings ($r \approx 180–230$ m, Figure 9 of that report) add a further limitation. If the structure is a 650 m impact crater in a porous target, as the regional geological model implies for the host, modeled shock pressure decays to 0.05–0.16 GPa at those outer-ring radii. The reference iron-impactor case gives 0.082 GPa at $r = 200$ m (§7.3). The impactor composition is a model assumption, and these values do not apply to specimens collected elsewhere in the structure. At the outer rings, such pressures would lie about two orders of magnitude below the ~10 GPa commonly cited for quartz PDF formation. The negative macroscopic results therefore describe the inspected specimens only. They neither confirm nor exclude a small carbonate-target impact.
3. **Two coordinates with different uses.** The paper places the structure at 25°44′59.31″N, 80°07′21.78″W on page 1. A coordinate on page 5, used for geological database searches, lies 266.9 m away. Neither coordinate identifies the precise location of a dive-gauge reading.
4. **Published and reconstructed water depths.** The authors report an 8.2 m gauge reading in the central zone and 5.65–6.00 m at three ridge stations. Combining the NOAA summit elevation with the Virginia Key noon and high-tide readings gives example depths of 6.06–6.17 m. The authors' Figure 4 is labeled a dive plan. When the plan is registered to H11898, five of six planned central markers fall beyond the pinnacle mapped in this study. The exact dive time, gauge offset and as-dived positions are unavailable. The depth model therefore cannot locate or invalidate their reported observation.
5. **The northeast comparison feature.** Registration of the authors' Figure 11 places its marked ridges in an area of positive relief on H11898 near the charted spoil ground. Figure 9C–D shows the registered position and the surrounding shelf profile. These data constrain the local surface geometry. The origin of the comparison feature requires independent evidence, as does the origin of the main structure.
6. **Scale of the geologic analogs (1,000 m Redwall pipes and 21–24 km rampart craters).** Paris et al. (their Fig. 10B) compare the structure with breccia pipes on the arid Colorado Plateau. These pipes reach about 1,000 m in depth and stoped upward from caverns in the Mississippian Redwall Limestone (Spencer, Wenrich, & Cole, 2015). They show that dissolution collapse can produce circular structures in limestone. Fluidized ejecta ramparts on Mars and at the Ries, 21–24 km in scale, are a further comparison case ($H_w / L < 0.4$ at MOCS, §7.2). Both analogs differ from this structure by about two orders of magnitude in target thickness or crater size. They indicate processes that can operate in carbonate or volatile-rich targets. Their geometry cannot be transferred directly to a structure of this size, and they do not decide its origin.

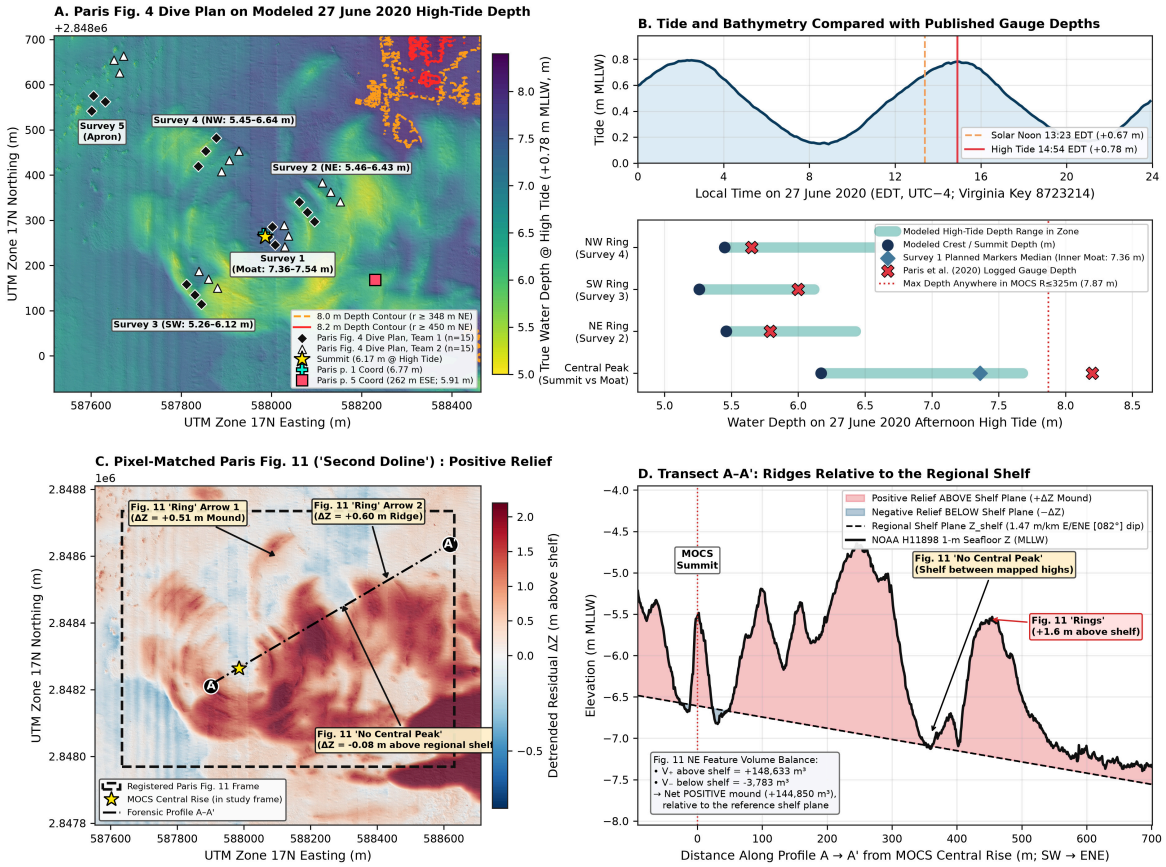

Figure 9. Comparison of the Paris et al. (2020) dive plan with mapped bathymetry. Panel A shows the registered planned stations over modeled afternoon high-tide water depths. Panel B compares the published gauge readings with example tide-adjusted depths. The planned markers do not establish as-dived positions. Panels C and D show the registration and topography of the northeast comparison feature. Positive relief within a spoil area is compatible with several origins.

6.1 What the Paris, Robertson and Schwartz field study establishes

Paris, Robertson and Schwartz (2020), of Planetary Sciences, Inc., examined 30 samples from 30 locations. Their specimens establish the presence of fossil-bearing oolitic limestone at the sampled surface locations, as expected under either dissolution or an impact into the regional carbonate target. They identified a genuine scaling problem for an ordinary complex crater with a central peak and multiple rings, compared regional dolines and acknowledged that the ENE outflow could record harbor dredging. Their inspections found no diagnostic shock features in the specimens and no meteoritic material in the proposed ejecta field.

I agree with their recommendation against listing the site in the Earth Impact Database and against using an unqualified crater label on Google Maps. The results do not by themselves establish a solutional doline. A sample from the surface cannot test for deeper brecciation across the summit. The reported central-zone gauge reading can coexist with a local mound in a broader depression. Figure 4 gives the dive plan without the as-dived positions necessary to identify the summit reading. The text places the comparison feature roughly 400 m northeast. Figure 11 marks ridges whose registered position on modern bathymetry shows local positive relief. That weakens the analogy to a depression without identifying the origin of either feature.

In my judgment, the scientific claim required revision before publication. A referee or editor should have asked the authors to present uneven dissolution as a working interpretation or supply evidence that distinguishes it from competing origins. Suitable evidence might include a cored dissolution or collapse structure beneath the summit, or a common-datum comparison showing that the proposed regional analogues share the diagnostic geometry in question. Without such a test, the field observations support withholding impact classification while leaving the geological origin open.

7. Cratering mechanics in layered shallow-marine targets and carbonate shock barometry (2023–2026)

7.1 The modeled relationship between a 650 m outer ring and a subdued central mound

In homogeneous targets on Earth, the gravity-controlled transition from simple bowl-shaped craters to complex craters with central peaks occurs near $D \approx 2$ km in sedimentary rocks and near $D \approx 4$ km in crystalline basement (Pike, 1985; Grieve, 1987; Melosh, 1989; Grieve & Pilkington, 1996; French, 1998; Kenkmann, Poelchau, & Wulf, 2014; cf. the lunar $D \geq 3$ km transition of Krüger, Hergarten, & Kenkmann, 2018). Central peaks in complex craters typically rise $h_{cp} \approx 0.02–0.04\ D$. At $D = 650$ m that would be 13–26 m. A homogeneous-target comparison therefore leaves the MOCS central rise unexplained. Earlier assessments treated this as the main mechanical difficulty for the impact hypothesis. The MOCS target is a water-saturated carbonate column in which weak upper layers overlie much stronger rock (Table 1, Figure 10). Layered targets of this kind are expected to crater differently below about 1 km diameter. The points below describe how an impact into this column could produce the observed geometry. They establish mechanical feasibility only. They do not show that an impact occurred:

1. **Nested concentric cratering (Quaide & Oberbeck, 1968; Ormö & Lindström, 2000; Prieur et al., 2018; Ormö et al., 2024):** Consider an impactor striking a weak upper layer of total thickness $t_{weak} = H_w + H_1$ above a much stronger substrate ($Y_2 / Y_1 \gg 5$). In this setting, crater form depends on D_{outer} / t_{weak}. Normal bowls form for $D / t_{weak} < 3.8–4.2$. Central-mound craters form for $4.2 < D / t_{weak} < 8.0$. Flat-floored craters form for 8.0–10, and nested concentric craters form for $D / t_{weak} > 10$. At MOCS, t_{weak} ranges from about 12 m (H_w = 0 m, lowstand) to 20 m (H_w = 8 m, shallow shelf). This gives $D_{outer} / t_{weak} = 32.5–54.2$, which is well inside the nested-crater field. In the impact scenario, the weak, high-porosity Miami Limestone ($Y_1 \approx 0.45$ MPa $< \rho_1\ g\ d_{tc} \approx 1.5–2.2$ MPa) would fail by rotational slumping along bedding and cementation horizons. This slumping would widen the cavity into a broad terraced outer crater ($D_{outer} \approx 650$ m). The strength of the calcrete-capped Fort Thompson Formation ($Y_2 \approx 14.0$ MPa $\gg \rho_2\ g\ d_{tc}$) would halt excavation and leave a nested inner bedrock crater. The modeled inner diameter is $D_{inner} = 267.1–299.6$ m, so D_outer / D_inner = 2.17–2.43. The schematic ratio used in section 8 is 2.52, and the fitted outer/inner ridge ratio is 2.64. Reported concentric-crater ratios are 1.95 ± 0.15 at Lockne (Ormö, Shuvalov, & Lindström, 2002; Ormö et al., 2024), 2.12 ± 0.18 at Kärdla, and 2.25 ± 0.25 at Neugrund. Lunar concentric craters give 2.15 ± 0.30 (Trang, Gillis-Davis, & Hawke, 2016). iSALE hydrocode concentric suites give 2.40 ± 0.35 (Prieur et al., 2018) (Figure 10B, Figure 12B). The modeled ratios fall within these reported ranges. The fitted ridge ratio of 2.64 lies at the upper end and falls only within the iSALE range. Collapse or dissolution concentrated at two stratigraphic contacts could also produce nested arcs. For this reason, the ratio serves as a consistency check and does not discriminate between origins by itself.
2. **Subdued central bedrock mound (1.2–1.5 m, $h/D \approx 0.002$) without a crystalline central uplift:** A complex-crater central peak would stand 15–25 m high. The MOCS central pinnacle rises only +1.41–1.56 m above its moat (h/D ≈ 0.002). In the four-layer saturated column (Table 1), the outer cavity would cut through the 12 m Miami Limestone. The ~275 m inner cavity would reach the impedance contacts between the Fort Thompson, Tamiami and Hawthorn units at 32–54 m depth. This places the inner cavity inside the Quaide–Oberbeck central-mound window ($D_{inner} / z \approx 5.0–8.0$). In that window, two effects can leave a low floor prominence: upward reflection of the shock from the stronger layer, and shear resistance beneath the crater center (Quaide & Oberbeck, 1968; Prieur et al., 2018). In 30%–45% porous saturated carbonate, shock-induced pore-water overpressure and acoustic fluidization would lower the effective friction ($\mu_{eff} \rightarrow 0.05–0.15$). This would further limit relief (Melosh & Ivanov, 1999; Wünnemann, Collins, & Melosh, 2006; Kenkmann et al., 2014). Later Pleistocene–Holocene wave planation and meteoric dissolution could have bevelled the softer surrounding calcarenite. Cemented breccia or impactite in the mound would have resisted this erosion and remained as positive relief (+81,975 m³ on the western half). No breccia or impactite has been confirmed in the mound. Differential cementation of a karst residual or a reef framework would also produce resistant positive relief. A core through the summit, logged for breccia, shock features and cement history, would separate these cases.

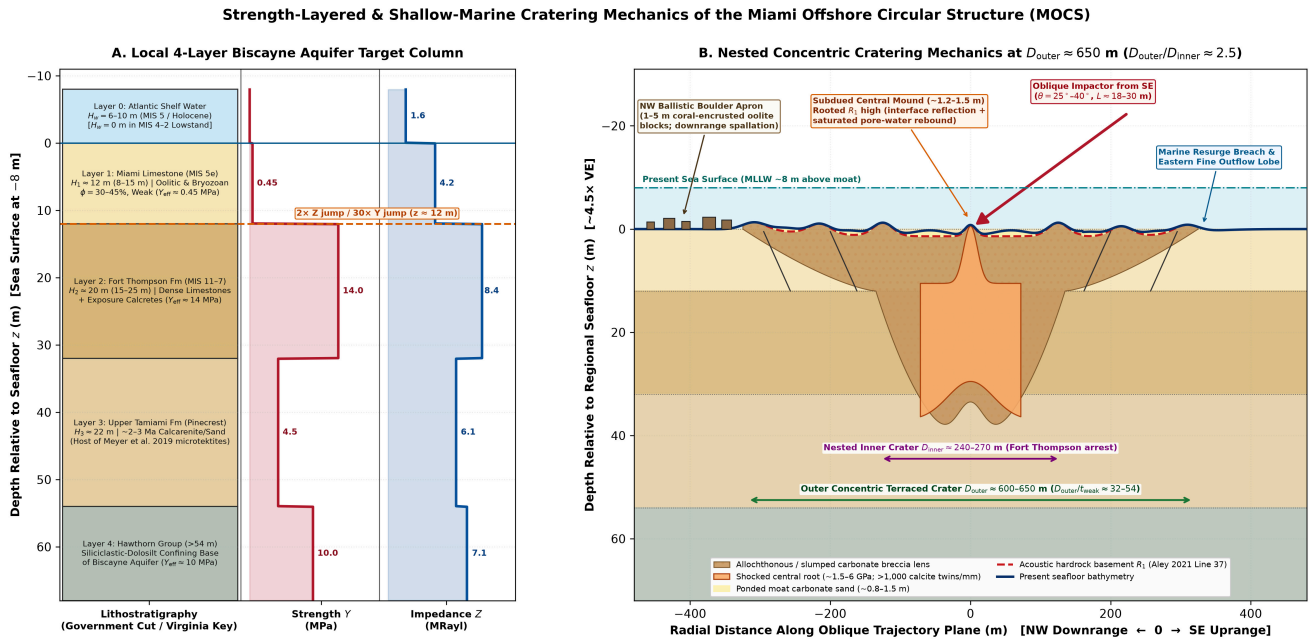

Figure 10. Strength-layered Biscayne Aquifer target column and nested concentric cratering mechanics at $D_{outer} \approx 650$ m. **(A)** Four-layer profile off Government Cut showing lithostratigraphy, yield strength (Y_{eff}) and acoustic impedance ($Z = \rho V_p$). At the Miami Limestone / Fort Thompson Formation unconformity (z ≈ 12 m), strength increases ~30× (0.45 → 14.0 MPa) and impedance increases 2.0× (4.20 → 8.40 MRayl). The panel also shows the chronostratigraphic separation of Layer 3. This is the ~2.0–3.2 Ma Pinecrest unit that hosts the microtektites reported by Meyer et al. (2019). **(B)** Schematic cross-section with ~4.5× vertical exaggeration along an assumed oblique SE→NW trajectory. The panel illustrates the impact scenario. It shows strength-arrested nested excavation ($D_{inner} \approx 240$–280 m inside $D_{outer} \approx 600$–650 m), formation of the subdued central mound (~1.2–1.5 m, drawn as rooted by assumption in the impact scenario), interpreted ballistic spallation downrange to the NW (H11898-28), and seaward breaching by resurge. Panel B is a conceptual model and does not depict imaged structure.

7.2 π-group scaling, shallow-marine energetics, oblique spallation and recurrence

The water-column drag deceleration of Collins, Melosh, & Marcus (2005) can be combined with the general strength–gravity π_D scaling of Holsapple (1993), Housen & Holsapple (2011) and Prieur et al. (2017). This gives:

$$v_{sf} = v_0 \exp\left(- \frac{3\rho_w C_D H_w}{4\rho_i L \sin\theta} \right) \tag{3}$$

$$\pi_D = \frac{D_{tc}}{(m_i / \rho_t)^{1/3}} = K_1 \left[\pi_2 \pi_4^{\frac{6\nu - 2 - \mu}{3\mu}} + \left(K_2 \pi_3 \pi_4^{\frac{6\nu - 2}{3\mu}} \right)^{\frac{2+\mu}{2}} \right]^{-\frac{\mu}{2+\mu}} (\sin\theta)^{1/3} \tag{4}$$

where $\pi_2 = g L / v_{sf}^2$, $\pi_3 = Y_{eff} / (\rho_t v_{sf}^2)$, and $\pi_4 = \rho_t / \rho_i$. The scaling was benchmarked against Barringer (Meteor) Crater using the decelerated intact-core parameters of Melosh & Collins (2005): L = 40 m iron, v = 12.8 km/s, 45°, $\rho_t = 2{,}300$ kg m^{-3} and $Y = 1.5$ MPa. These parameters give $D = 1{,}233.3$ m, compared with 1,186 m observed (+4.0%). Table 8 lists projectile solutions that reproduce $D_{outer} = 650$ m. The solutions span v_0 = 11–20 km/s, oblique entry angles θ = 20°–45°, and water depths of $H_w = 0$ m and 8 m (Figure 11A–B). These solutions assume an impact origin. They show which projectiles could produce a crater of the observed size, and they do not test whether an impact occurred.

Table 8. Strength-layered Holsapple/Collins projectile scaling and computed porous-carbonate shock-pressure radii for $D_{outer} = 650$ m at MOCS. Barringer benchmark: 1,233.3 m modeled vs. 1,186 m observed.

Impactor Composition	v_0 (km s^{-1})	Angle θ (°)	Water H_w (m)	Diameter L (m)	v_{sf} (km s^{-1})	H_w / L	Kinetic Energy E_k (kt / Mt TNT)	D_{inner} (m)	D_{outer} / D_{inner}	$P(r=45$ m) Hypothetical Central Root (GPa)	Modeled radius of the 3.9 GPa contour (m)
Iron (7,800 kg/m³)	11.0	30°	8.0	**26.0**	10.43	0.31	1,034 kt (1.03 Mt)	269.7	2.41	5.01	49.2
Iron (Reference)	**15.0**	**30°**	**8.0**	**22.6**	**14.11**	**0.35**	**1,268 kt (1.27 Mt)**	**275.2**	**2.36**	**5.76**	**51.7**
Iron (Lowstand)	15.0	30°	0.0	**23.5**	15.00	0.00	1,433 kt (1.43 Mt)	299.6	2.17	7.22	56.0
Iron (7,800 kg/m³)	15.0	45°	8.0	**19.5**	14.27	0.41	813 kt (0.81 Mt)	272.1	2.39	5.94	52.2
Iron (7,800 kg/m³)	15.0	20°	8.0	**26.6**	13.90	0.30	2,076 kt (2.08 Mt)	278.0	2.34	5.57	51.1
Iron (7,800 kg/m³)	20.0	30°	8.0	**19.9**	18.66	0.40	1,537 kt (1.54 Mt)	280.4	2.32	6.64	54.3
Stony (3,300 kg/m³)	15.0	30°	8.0	**32.7**	13.57	0.24	1,628 kt (1.63 Mt)	267.1	2.43	10.92	64.7
Stony (Reference)	**17.0**	**30°**	**8.0**	**31.0**	**15.30**	**0.26**	**1,771 kt (1.77 Mt)**	**268.5**	**2.42**	**11.53**	**65.8**
Stony (3,300 kg/m³)	20.0	45°	8.0	**24.7**	18.22	0.32	1,249 kt (1.25 Mt)	269.3	2.41	12.82	68.4

Table 8 has four quantitative implications for the impact scenario:

1. **Atmospheric filtering favors an iron impactor (L = 18.4–31.6 m):** Stony meteoroids 25–33 m across commonly fragment at 15–30 km altitude, where ram pressure exceeds their 1–5 MPa bulk strength. They tend to produce airbursts rather than single craters. Iron bodies 18–26 m across usually survive atmospheric passage intact (Collins et al., 2005; Bland & Artemieva, 2006). The reference iron in Table 8 is 22.6 m across at 15 km/s, 30° and H_w = 8 m, with E = 1,268 kt = 1.27 Mt TNT. An iron projectile is consistent with most confirmed terrestrial single craters 0.1–1.2 km in diameter, including Kaali, Henbury, Odessa, Boxhole, Monturaqui, Wolfe Creek and Barringer. The iron composition at MOCS is inferred from these survival arguments. It has not been confirmed by recovered projectile material.
2. **Shallow-marine regime (H_w / L = 0.24–0.41 < 1):** Marine impacts stop excavating the seabed only when $H_w / L \gtrsim 4$–6 (Ormö & Lindström, 2000; Ormö et al., 2002; Wünnemann, Weiss, & Hofmann, 2007). At $H_w = 8$ m, the 22.6 m reference iron loses only 5.9% of its velocity in the water column. This corresponds to 11.5% of its kinetic energy (19.0% for the 31.0 m stony reference), so 88.5% would reach the Miami Limestone. The model also predicts a strong resurge. The resurge would breach the seaward rim, carry carbonate mud eastward, and infill the floor (D/d ≈ 240). The seaward gap and the shallow floor are consistent with this prediction. Tidal scour, shoal migration and harbor dredging near Government Cut could also open a seaward gap and change floor depth. Floor cores could test for a graded resurge deposit above disturbed bedrock and help separate these explanations.
3. **Oblique SE→NW trajectory (θ = 20°–45°) and ballistic NW boulder emplacement:** Crater rims stay circular down to θ ≈ 12°–15°. Below θ ≈ 45°, ejecta curtains concentrate downrange (Gault & Wedekind, 1978; Pierazzo & Melosh, 2000; Elbeshausen, Wünnemann, & Collins, 2009; Kenkmann et al., 2014). For ballistic spall launched inside the vapor plume at ψ = 35°,

$$v_{ej}(R) = \sqrt{\frac{Rg}{\sin(2\psi)}} \quad (5)$$

the required launch speeds are modest: 72.2 m/s for R = 500 m, 91.4 m/s for R = 800 m, and 107.1 m/s for R = 1,100 m. These speeds would place 1–5 m blocks upslope across H11898-28. The SE→NW trajectory and the ballistic origin of these blocks are inferences. Dredge-spoil dumping is documented in the region. The positions of individual loads and the local construction history are unresolved. Several tests could evaluate the ballistic interpretation. The blocks could be compared petrographically with the local Fort Thompson section and with known dumped material, and they could be examined for shock features.

4. **Illustrative Florida-shelf Poisson recurrence (0.49%):** A 1.27 Mt top-of-atmosphere bolide strikes Earth once every ~168 yr (Brown et al., 2002). After atmospheric filtering, a single terrestrial crater with $D \geq 650$ m forms once every ~7,525 yr, or ~16.6 globally over 125 ka (Bland & Artemieva, 2006). Scaled to the 1.50×10^5 km² Florida carbonate shelf, the 125 ka Poisson expectation is 0.49%. Inside a 4,500 km² SE Florida multibeam strip, the expectation is 0.015%. Section 9 adopts P_0 = 0.50% as the baseline prior. This is one defensible choice among several, and the model weights in section 9 depend on it. With a 0.10% prior, paleokarst is favored. The 0.50% baseline favors impact only marginally.

7.3 Calcite twinning and modeled radial pressure decay

Classical shock barometers rely on silicate minerals such as quartz. They cannot be applied to pure carbonate, and their usefulness off Government Cut depends on the silicate content of bedrock that has not yet been sampled. Carbonate melt and decarbonation phases formed at high shock pressures (>30–60 GPa) also back-react rapidly in wet environments (Kieffer & Simonds, 1980; Agrinier et al., 2001; Osinski, Spray, & Grieve, 2008; French & Koeberl, 2010). Two recent studies examine calcite twinning as a low-shock indicator. Poelchau et al. (2025) report twin densities in marble shocked experimentally to 3.9 GPa peak pressure. Seybold et al. (2023) describe calcite twins in metagranite cataclasites from the crystalline Ries target. Neither study supplies a pressure calibration for cataclasites in a carbonate target. Cavosie et al. (2026) list calcite deformation twins as nonexclusive features, separate from accepted impact-diagnostic criteria. Twins can justify further petrography, but they cannot independently establish a shock origin.

- Poelchau et al. (2025, *Geology* 53(3): 279–283): The authors shocked marble experimentally and complemented the experiments with numerical modeling. In marble shocked to a peak pressure of 3.9 GPa and a shear stress of 1.4 GPa, calcite twin density can exceed 1,000 twins/mm. On average, the twins are narrower than the wavelength of visible light, which alters the optical properties of the shocked calcite. The modeling indicates that calcite can sustain shear stresses of ~1.4 GPa under highly dynamic loading. The authors propose calcite twin piezometry as a way to evaluate shock deformation in calcite. Shear stress and peak pressure are distinct physical quantities in this study.
- Seybold et al. (2023, *Meteoritics & Planetary Science* 58(9): 1287–1305): The authors studied calcite-bearing metagranite cataclasites from crystalline megablocks of the Ries impact structure and from cores of the FBN1973 research drilling. The calcite likely derives from pre-impact veins in the Variscan metagranites and gneisses, whereas the cataclasis is attributed to the Miocene impact. Quartz in the metagranite components lacks planar deformation features, which constrains peak shock pressure in this material to <7 GPa. The calcite shows twin densities of >1 twin per µm and twin widths <100 nm. Crosscutting *e*-, *f*-, and *r*-twins can occur within an individual grain, and interaction of *r*- and *f*-twins produces previously unrecorded a-type domains. From the high twin density and the activation of several twin systems in one grain, the authors infer differential stresses on the order of 1 GPa. This stress estimate is distinct from peak shock pressure. Because the host is a crystalline target, these results do not calibrate twinning in carbonate-target cataclasites.

To locate candidate sampling sites, this study adopts 1.5–5.0 GPa as an assumed scenario interval. It is not a pressure range calibrated by Poelchau et al. (2025) or Seybold et al. (2023). Under the reference iron-impact scenario and the attenuation law used here, the interval falls roughly 47–72 m from the source. The same calculation gives 5.76 GPa at 45 m and 0.082 GPa at 200 m (Figure 11C). These model outputs indicate where deformation could be sought if the impact hypothesis is correct. No shock pressure has been measured at Miami. High-density calcite twins would not by themselves demonstrate a shock origin. A positive result would require independent diagnostic evidence, such as mineral-specific shock features in any silicate grains present or carefully controlled geochemistry. A negative result would constrain only

the material sampled. The layering and properties of the carbonate host come from the regional geological model, and off-site borings establish material only at their own locations. A negative result would therefore not characterize the unsampled local bedrock.

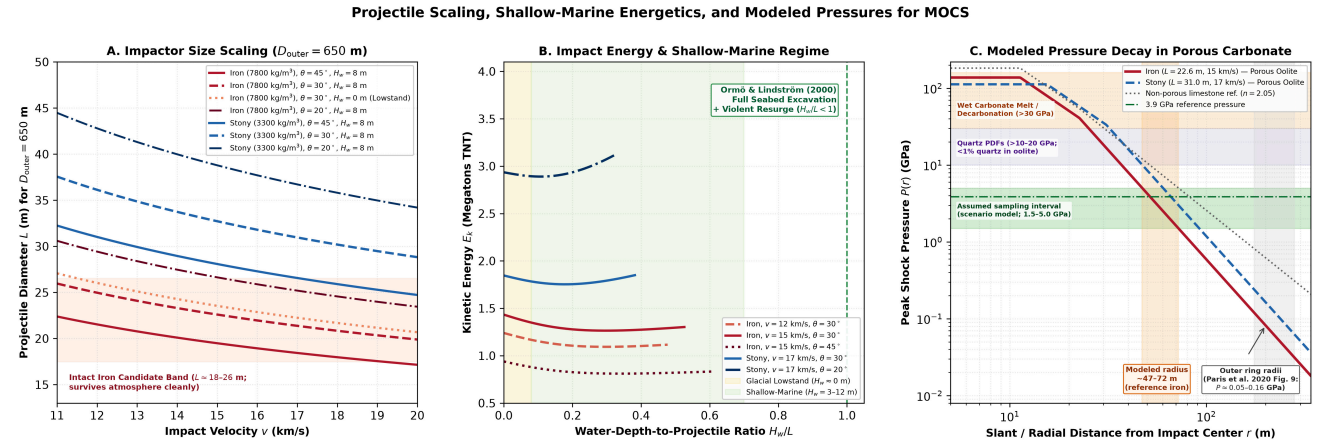

Figure 11. Projectile scaling for a strength-layered target, shallow-marine energetics, and shock decay in porous carbonate for $D_{\text{outer}} = 650$ m at MOCS. Target layering and porosity follow the regional geological model. **(A)** Impactor diameter $L(v_0)$ for iron (7,800 kg/m³) and stony (3,300 kg/m³) projectiles (θ = 20°–45°, H_w = 0–8 m). The shaded band marks the 18–26 m iron projectiles that survive atmospheric entry in the model. **(B)** Kinetic energy (megatons of TNT equivalent, Mt TNT) against the ratio of water depth to projectile diameter, H_w / L, for the modeled excavation and resurge scenario ($H_w / L = 0.24$–$0.41 \ll 1$). **(C)** Log–log plot of modeled radial shock decay $P(r)$. The 1.5–5.0 GPa interval, a scenario sampling range assumed here to locate candidate sites, falls at r ≈ 47–72 m. It is not a calibrated range from Poelchau et al. (2025) or Seybold et al. (2023). The modeled pressure is 5.76 GPa at r = 45 m, the position assigned to a hypothetical bedrock root beneath the Central Rise. No such root has been imaged. At the outer slump-ring radii (r ≈ 200 m), modeled pressures are only 0.05–0.16 GPa.

8. Endogenic alternatives involving Biscayne paleokarst chimneys and bioherm or shoal rings

The simple bowl model in Table 10 represents only one end member of the karst hypothesis. Paris et al. proposed uneven dissolution of the limestone, which can leave residual highs within a depression. Table 9 and Figure 12 compare MOCS quantitatively with documented submarine and onshore karst populations, mainly from Florida and the Bahamas (Mylroie, Carew, & Moore, 1995; Land, Paull, & Hobson, 1995; Tihansky, 1999; Land & Paull, 2000; Cunningham et al., 2006; Gischler, Anselmetti, & Shinn, 2013; NOAA Ocean Exploration, 2020; Patin et al., 2021).

Sections 8.1 and 8.2 evaluate the two strongest endogenic hypotheses. Each is given its most favorable physical mechanism and paired with the observation or test that would separate it from impact. Neither is ruled out by the present data. Mixed origins, such as a karst or shoal feature later modified by dredging or spoil placement, also remain credible but lie outside the mutually exclusive single-origin models compared here.

Table 9. Morphometric comparison of MOCS with documented karst landforms, mainly from Florida and the Bahamas, and with paleokarst sag pipes.

Karst / Candidate Feature	Geologic Setting & Host Unit	Diameter D (m)	Depth / Relief d (m)	Aspect Ratio D/d	Central Rise?	External Boulder Apron?	Primary Reference
Amberjack & Green Banana Holes	West Florida Shelf (34–47 m wd)	25–41	73–83	**0.38–0.49**	No	No	NOAA Ocean Exploration (2020); Patin et al. (2021)
Dean's & Great Blue Holes	Bahamas / Lighthouse Reef, Belize	25–318	124–202	**0.15–2.56**	No	No	Mylroie et al. (1995); Gischler et al. (2013)
Miami Rock Ridge Dolines	Onshore eogenetic Miami Limestone	5–25	1.5–5	**3–10**	No	No	Halley & Evans (1983); Cunningham et al. (2006)
Central FL Cover-Collapse	Hawthorn / Ocala karst (Winter Park)	70–150	29–67	**1.1–4.2**	No	No	Tihansky (1999)
Miami Terrace & Jordan Sinkholes	Deep Straits of Florida (250–365 m wd)	220–575	25–180	**3.19–8.8**	No	No	Land et al. (1995); Land & Paull (2000)
Biscayne Bay Seismic-Sag Pipes	Deep Floridan–Pleistocene sag columns	150–500	8–35 *(sag)*	**12–30**	No *(sag)*	No	Cunningham (2015); Cunningham et al. (2018)
Kanab UT Breccia Pipe *(analog from a different setting)*	Colorado Plateau (~1 km Redwall root)	220	28	**7.9**	No	No	Spencer, Wenrich, & Cole (2015)
MOCS (Apparent Seabed)	Inner-shelf Miami Limestone (5.4–7 m)	**650** *(in. 250)*	**~2.7** *(R1 ~3.8)*	**~240** *(in. ~66)*	**Yes (+1.56 m)** *(seabed relief, root not imaged)*	**Yes (H11898-28)**	Reynolds (2009); Aley (2021); This study

8.1 Compound Biscayne paleokarst with differential calcrete cementation (H_2)

A simple cavern collapse is mechanically unlikely. A 12 m-thick eogenetic oolite with a strength of 3 MPa is unlikely to span an unsupported cavern roof 650 m across, a span-to-thickness ratio of about 54:1 (Waltham, Bell, & Culshaw, 2005). A deeper mechanism has stronger support. Cunningham (2015) and Cunningham et al. (2018) used 2D and 3D seismic reflection surveys across Biscayne Bay and southeastern Miami-Dade County to document columnar hypogene or paleokarst seismic-sag structures with D = 150–500+ m. These structures are rooted hundreds of meters deep in Eocene–Oligocene limestones of the Floridan Aquifer, including the "Boulder Zone". They propagate upward through the Hawthorn Group and produce gentle sagging in the overlying Pleistocene strata.

In this scenario (H_2), several processes act in sequence. During the -120 m Wisconsinan lowstand, vadose calcrete could have case-hardened the rock in steps along concentric sag fractures, with cementation varying across the porous, layered host. Holocene sediment could then have filled the depression and raised the aspect ratio toward D/d → 240. Stray iron from port activity or spoil, an inferred source, could account for the magnetic signal (E6). Uneven dissolution of the kind proposed by Paris et al. could, in principle, also leave a residual central high.

H_2 has two main misfits. First, sag pipes typically show their greatest subsidence at the center, whereas MOCS has a central rise (E2). Uneven dissolution weakens this misfit somewhat, although it does not obviously predict a rise at the center itself. Second, inward karst transport does not readily place material outside the structure. A separate hardbottom outcrop west of Area 3 could account for the northwest apron (E4) under H_2. Whether its blocks originated in the structure is unknown.

The proposed Stage-1 Boomer seismic survey, with 30–100 m penetration, could help separate H_2 from some impact scenarios. H_2 predicts reflectors that sag downward more than 60–200 m into Hawthorn and Floridan strata. The deeper part of that range exceeds the nominal penetration, so the test depends on resolution and reflector geometry. A shallow reflector that ends beneath the summit would not by itself indicate a root, uplift or bedrock.

8.2 A buried bioherm, patch reef or cemented ooid-shoal ring (H_3)

P. V. Heinrich compared MOCS with the circular Lower Cretaceous Edwards Limestone rudist bioherms at Childress Creek, Texas, mapped by Roberson (1972). In this scenario (H_3), frame-building organisms grew around a periphery, or meteoric calcrete unevenly cemented the arcuate crests of an MIS 5e/7 patch reef or ooid shoal (Hoffmeister et al., 1967; Halley & Evans, 1983; Neal et al., 2008). Either process would build ring volume above the shelf plane and produce a high aspect ratio, $D/d \approx 240$. Reef growth, shoal development and differential cementation are all expected in this carbonate setting, which makes H_3 a serious alternative.

Three observations fit H_3 poorly. First, MOCS lies landward of the shelf-margin reef tract, within oolitic grainstone that contains lagoonal gastropods (*Modulus modulus*, *Cerithium litteratum*; Paris, Robertson, & Schwartz, 2020). Second, the regional Miami ooid bars are linear or parabolic and do not form concentric rings around a central high. Third, if the NW boulders derive from the structure, bioherms provide no mechanism for a one-sided apron extending 1.65 km.

The proposed Stage-3 rotary rock coring would test H_3 directly. Primary boundstone or undisturbed cross-bedding beneath the ridges would support a reef or shoal origin. The absence of these fabrics in a limited number of cores would weaken H_3 without by itself establishing impact.

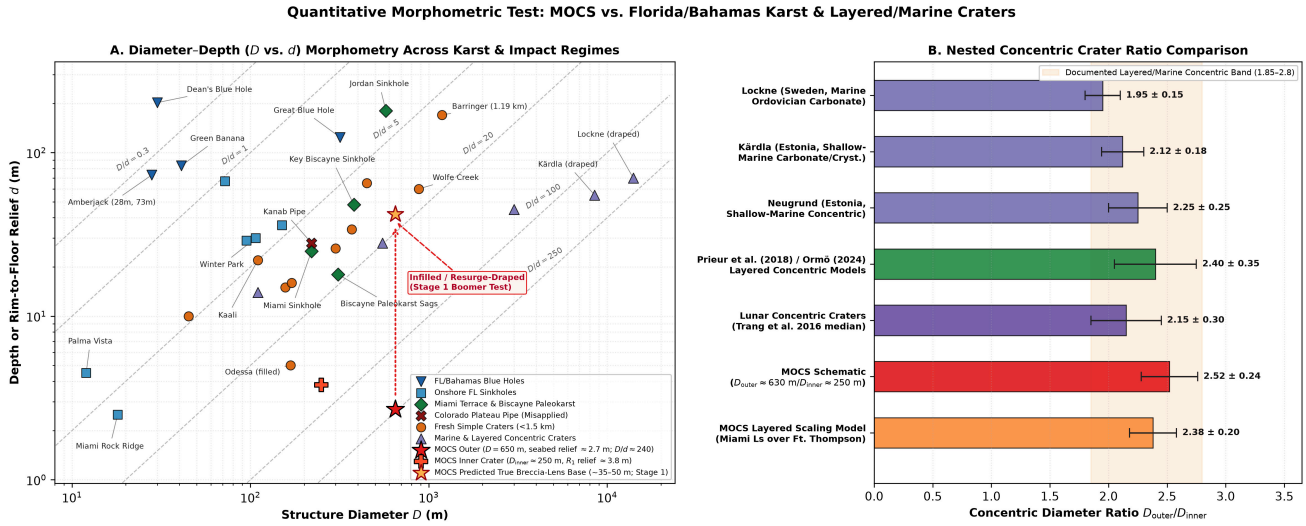

Figure 12. Panel A compares the surface relief and span of the structure with selected karst examples. Different definitions of relief, depth and diameter affect this comparison. Panel B uses nominal spans of 630 and 250 m, giving a ratio of 2.52. This is a schematic pair with an assigned spread and is separate from the fitted ridges in Table 2. The fitted outer/inner ridge ratio is 270.26 / 102.56 = 2.64. Using the basal perimeter and the inner ridge instead gives 577.50 / 205.11 = 2.82. The ratio depends on the choice of boundaries and cannot by itself diagnose origin.

9. Sensitivity of the five-hypothesis model

Five origin scenarios are compared across eight observational lines (E1–E8, Table 10):

- H_1, a candidate oblique impact into layered carbonate targets.
- H_2, a compound Biscayne paleokarst chimney with differential cementation and unrelated iron sources.
- H_3, a circular bioherm or cemented ooid-shoal ring.
- H_4, a simple single-stage doline (Paris et al., 2020).
- H_5, a primary dredge-spoil or explosion architecture.

The update uses correlation-tempered Bayes weighting with $\alpha = 0.80$ (Equation 6), applied equally to every hypothesis. The damping limits double counting of the correlated geomorphic observations (E1–E3). Ambiguous anthropogenic and sedimentological signals (E5–E6) receive modest likelihood contrasts in Table 10 for the same reason.

Each likelihood in Table 10 is an assigned judgment, not a frequency estimated from a validated sample of known sites. The regional prior is a modeling assumption about the chance of an impact somewhere on the shelf, which differs from the chance that this particular feature is an impact structure. The ranking is sensitive to that assumption. The 0.50 percent baseline prior marginally favors impact, whereas a 0.10 percent prior favors paleokarst. The scenarios are treated as mutually exclusive, so mixed origins, such as stable dredge deposits placed over inherited relief, are omitted. The model also does not use the 1934–35 survey comparison. The resulting weights describe the behavior of the model under these inputs and are not measured odds.

$$P(H_j \mid E) = \frac{P_0(H_j)\left[\prod_{k=1}^{8} P(E_k \mid H_j)\right]^{\alpha}}{\sum_{m=1}^{5} P_0(H_m)\left[\prod_{k=1}^{8} P(E_k \mid H_m)\right]^{\alpha}}, \qquad \alpha = 0.80 \tag{6}$$

Each likelihood entry was perturbed with a log-normal uncertainty of $\sigma_{ln} = \pm 0.40$ (approximately 1.5× at 1σ) over 10,000 Monte Carlo realizations. The prior was held at the assumed 125-ka Florida-Shelf baseline, $P_0(H_1) = 0.50\%$, with $P_0[H_2..H_5] = [36.5\%, 18.0\%, 30.0\%, 15.0\%]$. The resulting intervals reflect likelihood uncertainty only and exclude uncertainty in the prior and the model structure. The results are (Table 11, Figure 13A):

- H_1, candidate oblique layered impact: 52.1% (90% Monte Carlo interval 12.8%–86.2%)
- H_2 and H_3, the two strongest endogenic alternatives (47.9% combined): compound Biscayne paleokarst chimney 26.9% (90% interval 4.5%–68.1%) and circular bioherm or shoal ring 21.0% (90% interval 3.3%–58.0%)
- H_4, simple single-stage solutional doline (Paris et al., 2020): <0.01% (0.004% point estimate, 0.003% Monte Carlo median). The Bayes factor (BF) is untempered $\log_{10}\mathrm{BF}[H_1/H_4] = +7.43$ and tempered +5.94.
- H_5, primary dredge-spoil or explosion architecture: 0.01% (0.006% point estimate, 0.005% Monte Carlo median). The Bayes factor is untempered $\log_{10}\mathrm{BF}[H_1/H_5] = +6.77$ and tempered +5.42. This low weight applies to spoil or blasting as the primary builder of the structure. It does not evaluate spoil placed over pre-existing relief.

Table 10. Eight-observation likelihood matrix $P(E_k \mid H_j)$ for the five origin hypotheses, with the rationale assigned to each entry. All entries are assigned judgments. E5 and E6 are weighted conservatively because of overlap with Area 3 spoil and because the VB-DA20-24 sample shows comparable shelf mud.

ID	Observation & Metric	H_1 Impact	H_2 Paleokarst	H_3 Bioherm	H_4 Simple Doline	H_5 Primary Spoil (end-member)	Rationale for Assigned Likelihoods (author judgment)
E1	Concentric multi-ring planform (Rings R1–R3, shallow picked horizon)	0.72	0.22	0.28	0.030	0.008	Strength-layered craters predict nested rings (Do/Di ≈ 2.4). Possible in a cemented sag or bioherm. Assigned low for primary spoil because the loose mound rows (Line 42) lack rings. Local reworking is not excluded.
E2	Central rise (+1.41–1.56 m above moat). The model treats it as rooted, but Reflector R1 on Line 37 is unpicked beneath the summit.	0.58	0.14	0.16	0.015	0.010	The assigned weight assumes a subdued central uplift in a layered, saturated target (h/D ≈ 0.002). A root has not been imaged. Uneven dissolution or reef growth could leave a central high. A simple collapse bowl (H4) predicts a central low.
E3	High aspect ratio (D/d ≈ 240, V_{net} = +81,975 m³ on W half) vs. FL karst	0.68	0.28	0.45	0.025	0.150	Consistent with planed or resurge-draped marine craters and with shoal rings. H2 requires substantial infill. Broader than FL blue holes and dolines (0.15–10). The uneven dissolution proposed by Paris et al. need not follow simple-doline proportions.
E4	Unilateral NW calcareous/coral boulder apron (H11898-28, outside Area 3)	0.75	0.09	0.12	0.008	0.080	Weight assumes SE→NW oblique-impact spallation, which is unverified. Karst collapse tends to move debris inward. The apron lies outside 1973 Area 3 and lacks the 87.6° E–W mound rows. Undocumented local placement or reworking of carbonate spoil is not excluded. Block provenance is unresolved.
E5	Eastern rim low & 23.8%–29.0% fines (VB-DA20-30/-31 vs. 8.9–14% & 22.3% in -24)	0.62	0.48	0.35	0.300	0.400	Low discrimination. Consistent with resurge rock flour, a harbor ebb plume or pre-1975 Area 3 fine spoil. The off-structure core VB-DA20-24 also has 22.3% fines.
E6	Five ring clusters (six symbols) (M01–M02, M04–M07) + 20 E-lobe picks (0 on peak/NW)	0.55	0.32	0.25	0.080	0.350	Low discrimination. Fe–Ni or oxide remnants are one possible source. Amplitudes (nT) are unpublished. M26 and M16–M20 are compatible with port-related ferrous debris. Source composition is inferred.
E7	Carbonate lithology in cores and grabs (no concrete or foreign slag observed)	0.80	0.82	0.82	0.820	0.060	Expected for natural carbonate breccia, karst or a bioherm, and consistent with locally dredged carbonate. The low H5 weight assumes heterogeneous port spoil.
E8	No diagnostic shock features reported in the Paris et al. (2020) specimens	0.78	0.95	0.95	0.950	0.950	Model assumes limited sensitivity for outer-ring material ($P \approx 0.082$ GPa at 200 m in the reference scenario). The team also sampled other zones. No systematic thin-section grain counts or modal proportions for the 30 samples are reported.

Table 11. Sensitivity of posterior probabilities to the prior assignment $P_0(H_1)$. Under the assumed 0.50% 125-ka Florida-Shelf Poisson baseline, the point model ranks H_1 first (52.1%) and H_2 second (26.9%). Ninety-percent intervals from 10,000 Monte Carlo trials show the effect of likelihood uncertainty at that baseline. These intervals are wide compared with the point-model margin between H_1 and H_2 and exclude uncertainty in the prior and model structure. Under the 0.10% strict southeast Florida corridor prior, H_2 ranks first (46.5%) and H_1 falls to 17.8%.

Prior scenario	$P_0(H_1)$	$P(H_1$ Impact)	$P(H_2$ Paleokarst)	$P(H_3$ Bioherm/Shoal)	$P(H_4$ Simple Doline)	$P(H_5$ Primary Spoil)
Strict SE-FL Corridor Prior (4,500 km², α=0.80)	0.10%	17.8%	**46.5%**	35.8%	0.006%	0.01%
FL-Shelf 125-ka Poisson Baseline (α=0.80)	**0.50%**	**52.1%** *(12.8–86.2%)*	**26.9%** *(4.5–68.1%)*	**21.0%** *(3.3–58.0%)*	**<0.01%** *(0.004%)*	**0.01%** *(0.006%)*
FL-Shelf Poisson Untempered (α=1.00)	0.50%	78.1%	11.7%	10.2%	<0.001%	<0.001%
Anomaly-Conditioned Shelf Prior (α=0.80)	2.00%	81.7%	10.3%	8.0%	0.001%	0.004%
Uniform Uninformed 5-Way Prior (α=0.80)	20.0%	98.2%	0.7%	1.1%	<0.001%	<0.001%

10. Proposed South Florida field and laboratory tests

Figure 13B and Table 12 outline a possible investigation. It begins by mapping the distribution and thickness of placed material and the geology beneath it. The host rock shapes the design. The regional model places porous Miami Limestone over a stronger carbonate unit. Local cementation and the depth of the contact beneath the summit need direct measurement. Each stage is designed to yield results that can discriminate among endogenic, anthropogenic, mixed and impact origins. Sample work would look for mineral-specific diagnostic shock features and would use carefully controlled geochemistry, interpreted against local carbonate heterogeneity. None of this work has been approved or completed, and the costs are planning estimates. No project-specific permit, exemption, committed vessel, institutional partnership or funding is documented. Before any work, the sponsor would need to confirm jurisdiction, access, protected-habitat constraints and the requirements for each method.

Table 12. Proposed work, possible interpretations and planning costs. For each stage, the table lists results that would favor an alternative and results that would warrant follow-up. Diagnostic claims follow the Meteoritical Society Impact Cratering Committee (Cavosie et al., 2026).

Stage	Method	Proposed sites or materials	Evidence favoring an alternative	Evidence warranting follow-up	Estimated cost (USD)
1. Seismic profiles	Acquire a grid with greater penetration and off-structure tie lines.	Ring system and northeast control area	Deep sagging or a dissolution pipe favors collapse.	Map a bounded basin, possible breccia lens or uplift. Check against stratigraphy.	18,000–35,000
2. Magnetic mapping	Tight-grid gradiometry and, where authorized, small sediment samples.	Northwest apron, anomaly targets and background sites	Modern debris associated with targets supports a local human source.	Buried targets can guide sampling. Shape and intensity cannot establish composition.	15,000–28,000
3. Bedrock cores	Recover continuous, oriented sections across contacts.	Center, moat, ridge, apron and control sites	Intact reef, karst fill, placed rubble or disposal-age sediment can identify local processes.	A coherent breccia or unusual mineral assemblage can justify controlled laboratory tests.	42,000–85,000
4. Petrography	Polished thin sections, SEM-EBSD and quartz-residue characterization.	Bedrock and breccia with documented position and comparison samples	Absence of diagnostic features limits conclusions to the sampled material.	High-density calcite twins alone are insufficient. Seek independently verified diagnostic shock features such as crystallographically indexed quartz PDFs.	12,000–25,000
5. Geochemistry and dating	Platinum-group elements, osmium isotopes and dating of appropriate material.	Breccia, controls, cements and coral	Local background and industrial contamination must be characterized.	A robust extraterrestrial signal in demonstrably related material, with spatial and temporal context, may establish projectile input. Dating a coral or cement dates that material.	15,000–30,000

Stages 1 and 2 are estimated at USD 33,000–63,000, and all five stages together at USD 102,000–203,000. Cost, access and the availability of diagnostic samples remain unresolved.

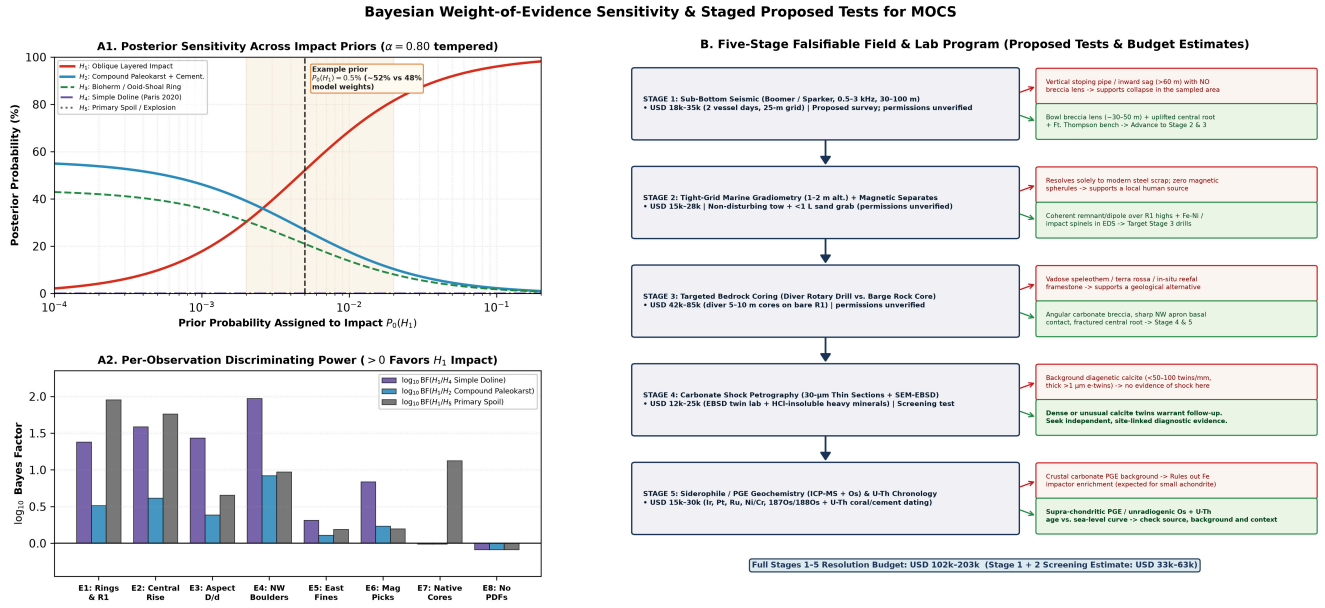

Figure 13. Sensitivity of the model to the selected prior and likelihoods (A1, A2), with a proposed sequence of surveys and tests (B). The baseline H_1 weight of 52.1% is a model output of the assigned correlated likelihoods, priors and model structure. A 0.10 percent impact prior favors paleokarst, while the 0.50 percent baseline marginally favors impact. Costs in B are planning estimates.

11. Conclusion

Repeat bathymetry fixes the modern ring geometry off Government Cut. The 1997 soundings match much of today's relief. The 1934–35 survey did not sound the summit and often shows smaller relief on the western crests. Disposal south of the channel is documented regionally, but individual loads and the mound's construction history are unresolved. The published flank-reflector pick does not extend across the summit. Surface samples lack diagnostic shocked rock, a result limited to the sampled material.

Among the five single-origin scenarios, I favor impact as the working hypothesis under the baseline 0.50 percent prior. That preference depends on the model and shifts to paleokarst at 0.10 percent. The weights record assumptions and cannot classify the site. Nothing observed so far excludes impact, and nothing site-specific confirms it. Reef growth or karst later modified by disposal also remains credible.

Two field tests could discriminate among these mechanisms. Cores through the summit and one ring crest, reaching the stronger lower unit, could reveal intact reef framework, karst fill, placed rubble with disposal-age sediment, or breccia bearing mineral-specific shock features. Sub-bottom profiles across the summit would show whether the reflector sags, continues beneath the rise or is disrupted by a bounded basin or uplift. If independent diagnostic evidence establishes impact, this site could help researchers recognize other small marine impacts in porous, layered carbonate. Evidence for dissolution, carbonate growth or emplacement would instead explain which features can mimic one.

Acknowledgments

Public hydrographic, topobathymetric LiDAR, tidal and marine mineral datasets made both the May 2012 identification of the feature and this quantitative synthesis possible. These datasets are archived by NOAA (Office of Coast Survey, National Centers for Environmental Information, National Geodetic Survey, and Center for Operational Oceanographic Products and Services), the U.S. Army Corps of Engineers (Jacksonville District and JALBTCX), and the Bureau of Ocean

Energy Management (MMIS / GeoSeas). Several people and organizations provided constraints used in this evaluation. They include Glikson, for early comments, and Heinrich, for the recorded bioherm comparison. C. O'Dale (*Crater Explorer*) preserved archival material. A. J. Paris, R. Robertson and S. Schwartz conducted underwater reconnaissance (2020). W. C. Aley IV and Taylor Engineering, Inc. presented regional marine geophysical results (2021). These acknowledgments do not imply endorsement of the interpretations in this paper.

Data Availability

Federal data and survey records include the following. NOAA Hydrographic Survey H11898 (H11898_MB_1m_MLLW_2of5.bag, H11898_Rky_Area_North, H11898_Spoil_Area_North, and Descriptive Report OPR-H328-OS-08-C). NOAA/JALBTCX H11870 (2008). USACE NCMP (2016, Mission 6196). FEMA/USACE Post-Irma (2017, Mission 8388). NOAA NGS Topobathy LiDAR (2017, Mission 8728, and 2018–2019, Mission 9060). Historical surveys H-4075/H-4088a (1919), H-4801 (1928), H-5727 (1935) and H-10748 (1997). Verified water levels from NOAA NWLON Station 8723214 (Virginia Key). BOEM MMIS / GeoSeas Study USACE_M20PG00014_StateWaters (survey_tracklines.json, core_samples.json, sand_resources.json). Python analysis scripts and machine-readable JSON outputs accompany the Version 4.0 research repository. The public paper and explorer are available at https://coryboehne.com/crater/ . The historical matched soundings and the 1935 review are linked from the explorer. The April 2021 Taylor Engineering county report provides project methods, core logs and laboratory samples. The public record also includes the Paris et al. article, the Aley conference slides and the original H05727 hydrographic review.

References

Agrinier, P., Deutsch, A., Schärer, U., & Martinez, I. (2001). Fast back-reactions of shock-released CO_2 from carbonates: An experimental approach. *Geochimica et Cosmochimica Acta*, 65(15), 2615–2632. https://doi.org/10.1016/S0016-7037(01)00617-2

Cavosie, A. J., et al. (2026). Impact-diagnostic criteria for use in confirming a meteorite impact origin of terrestrial geological structures. Recommendations by the Impact Cratering Committee of the Meteoritical Society. *Meteoritics & Planetary Science*. https://doi.org/10.1111/maps.70163

Aley, W. C., IV (2021). *A Meteorite Impact in Coastal Waters off Miami Beach? – Novel Data and Insights*. Presentation at the 34th Annual Florida Shore & Beach Preservation Association (FSBPA) National Conference on Beach Preservation Technology, February 5, 2021 (Taylor Engineering, Inc., 24 slides).

Blakely, R. J. (1995). *Potential Theory in Gravity and Magnetic Applications* (441 pp.). Cambridge University Press. https://doi.org/10.1017/CBO9780511549816

Bland, P. A., & Artemieva, N. A. (2006). The rate of small impacts on Earth. *Meteoritics & Planetary Science*, 41(4), 607–631. https://doi.org/10.1111/j.1945-5100.2006.tb00485.x

Boehne, C., & O'Dale, C. (2012). *The Miami, Florida Structure* (discovered May 11, 2012 in NOAA Survey H11898; archived history of the proposal and later geological comments, 2012–2015). *Crater Explorer* (https://craterexplorer.ca/miami-florida-structure/).

BOEM (Bureau of Ocean Energy Management) (2024). *Marine Minerals Information System (MMIS / GeoSeas) Geospatial Database: Offshore Miami-Dade Survey Tracklines (survey_tracklines.json), Vibracore Records (core_samples.json), and Sand Resource Polygons (sand_resources.json), StudyID USACE_M20PG00014_StateWaters*. U.S. Department of the Interior.

Breiner, S. (1973). *Applications Manual for Portable Magnetometers* (58 pp.). GeoMetrics, Sunnyvale, CA.

Brown, P., Spalding, R. E., ReVelle, D. O., Tagliaferri, E., & Worden, S. P. (2002). The flux of small near-Earth objects colliding with the Earth. *Nature*, 420(6913), 294–296. https://doi.org/10.1038/nature01238

Collins, G. S., Melosh, H. J., & Marcus, R. A. (2005). Earth Impact Effects Program: A Web-based computer program for calculating the regional environmental consequences of a meteoroid impact on Earth. *Meteoritics & Planetary Science*, 40(6), 817–840. https://doi.org/10.1111/j.1945-5100.2005.tb00157.x

Cunningham, K. J., Renken, R. A., Wacker, M. A., Zygnerski, M. R., Robinson, E., Shapiro, A. M., & Wingard, G. L. (2006). Application of carbonate cyclostratigraphy and borehole geophysics to delineate porosity and preferential flow in the karst limestone of the Biscayne aquifer, SE Florida. In R. S. Harmon & C. M. Wicks (Eds.), *Perspectives on Karst Geomorphology, Hydrology, and Geochemistry* (Geological Society of America Special Paper 404, pp. 191–208). https://doi.org/10.1130/2006.2404(16)

Cunningham, K. J., Sukop, M. C., Huang, H., Alvarez, P. F., Curran, H. A., Renken, R. A., & Dixon, J. F. (2009). Prominence of ichnologically influenced macroporosity in the karst Biscayne aquifer: Stratiform "super-K" zones. *Geological Society of America Bulletin*, 121(1–2), 164–180. https://doi.org/10.1130/B26392.1

Cunningham, K. J. (2015). *Seismic-sequence stratigraphy and geologic structure of the Floridan aquifer system near "Boulder Zone" deep wells in Miami-Dade County, Florida* (U.S. Geological Survey Scientific Investigations Report 2015–5013, 28 pp.). https://doi.org/10.3133/sir20155013

Cunningham, K. J., Dixon, J. F., Westcott, R. L., Norgard, S., & Walker, C. (2018). *Three-dimensional seismic characterization of karst in the Floridan aquifer system, southeastern Miami-Dade County, Florida* (U.S. Geological Survey Scientific Investigations Report 2018–5117, 19 pp.). https://doi.org/10.3133/sir20185117

Duane, D. B., & Meisburger, E. P. (1969). *Geomorphology and Sediments of the Nearshore Continental Shelf, Miami to Palm Beach, Florida* (Technical Memorandum No. 29, 47 pp.). U.S. Army Corps of Engineers, Coastal Engineering Research Center.

Elbeshausen, D., Wünnemann, K., & Collins, G. S. (2009). Scaling of oblique impacts in frictional targets: Implications for crater size and formation mechanisms. *Icarus*, 204(2), 716–731. https://doi.org/10.1016/j.icarus.2009.07.018

Fish, J. E., & Stewart, M. (1991). *Hydrogeology of the surficial aquifer system, Dade County, Florida* (U.S. Geological Survey Water-Resources Investigations Report 90–4108, 50 pp.). https://doi.org/10.3133/wri904108

French, B. M. (1998). *Traces of Catastrophe: A Handbook of Shock-Metamorphic Effects in Terrestrial Meteorite Impact Structures* (LPI Contribution No. 954, 120 pp.). Lunar and Planetary Institute.

French, B. M., & Koeberl, C. (2010). The convincing identification of terrestrial meteorite impact structures: What works, what doesn't, and why. *Earth-Science Reviews*, 98(1–2), 123–170. https://doi.org/10.1016/j.earscirev.2009.10.009

Gault, D. E., & Wedekind, J. A. (1978). Experimental studies of oblique impact. *Proceedings of the 9th Lunar and Planetary Science Conference*, 3843–3875.

Gischler, E., Anselmetti, F. S., & Shinn, E. A. (2013). Seismic stratigraphy of the Blue Hole (Lighthouse Reef, Belize), a late Holocene climate and storm archive. *Marine Geology*, 344, 155–162. https://doi.org/10.1016/j.margeo.2013.07.013

Grieve, R. A. F. (1987). Terrestrial impact structures. *Annual Review of Earth and Planetary Sciences*, 15, 245–270. https://doi.org/10.1146/annurev.ea.15.050187.001333

Grieve, R. A. F., & Pilkington, M. (1996). The signature of terrestrial impacts. *AGSO Journal of Australian Geology & Geophysics*, 16(4), 399–420.

Halley, R. B., & Evans, C. C. (1983). *The Miami Limestone: A Guide to Selected Outcrops and Their Interpretation* (67 pp.). Miami Geological Society.

Hoffmeister, J. E., Stockman, K. W., & Multer, H. G. (1967). Miami Limestone of Florida and its Recent Bahamian counterpart. *Geological Society of America Bulletin*, 78(2), 175–190. https://doi.org/10.1130/0016-7606(1967)78%5B175:MLOFAI%5D2.0.CO;2

Hoffmeister, J. E. (1974). *Land from the Sea: The Geologic Story of South Florida* (143 pp.). University of Miami Press.

Holsapple, K. A. (1993). The scaling of impact processes in planetary sciences. *Annual Review of Earth and Planetary Sciences*, 21, 333–373. https://doi.org/10.1146/annurev.ea.21.050193.002001

Housen, K. R., & Holsapple, K. A. (2011). Ejecta from impact craters. *Icarus*, 211(1), 856–875. https://doi.org/10.1016/j.icarus.2010.09.017

JALBTCX (Joint Airborne Lidar Bathymetry Technical Center of Expertise) (2008). *Hydrographic Survey Registry No. H11870: 2008 Airborne Bathymetric LiDAR Survey, Miami to Key Biscayne, Florida (H11870_LI_3m_MLLW_1of1.bag)*. NOAA Office of Coast Survey / NCEI.

Kenkmann, T., Poelchau, M. H., & Wulf, G. (2014). Structural geology of impact craters. *Journal of Structural Geology*, 62, 156–182. https://doi.org/10.1016/j.jsg.2014.01.015

Kieffer, S. W., & Simonds, C. H. (1980). The role of volatiles and lithology in the impact cratering process. *Reviews of Geophysics*, 18(1), 143–181. https://doi.org/10.1029/RG018i001p00143

Krüger, T., Hergarten, S., & Kenkmann, T. (2018). Deriving morphometric parameters and the simple-to-complex transition diameter from a high-resolution, global database of fresh lunar impact craters ($D \geq \sim 3$ km). *Journal of Geophysical Research: Planets*, 123(10), 2667–2690. https://doi.org/10.1029/2018JE005545

Land, L. A., Paull, C. K., & Hobson, B. (1995). Genesis of a submarine sinkhole without subaerial exposure: Straits of Florida. *Geology*, 23(10), 949–951. https://doi.org/10.1130/0091-7613(1995)023%3C0949:GOASSW%3E2.3.CO;2

Land, L. A., & Paull, C. K. (2000). Submarine karst belt rimming the continental slope in the Straits of Florida. *Geo-Marine Letters*, 20(2), 123–132. https://doi.org/10.1007/s003670000041

Melosh, H. J. (1989). *Impact Cratering: A Geologic Process* (245 pp.). Oxford University Press.

Melosh, H. J., & Ivanov, B. A. (1999). Impact crater collapse. *Annual Review of Earth and Planetary Sciences*, 27, 385–415. https://doi.org/10.1146/annurev.earth.27.1.385

Melosh, H. J., & Collins, G. S. (2005). Planetary science: Meteor Crater formed by low-velocity impact. *Nature*, 434(7030), 157. https://doi.org/10.1038/434157a

Meyer, M. B., Harries, P. J., & Portell, R. W. (2019). A first report of microtektites from the shell beds of southwestern Florida. *Meteoritics & Planetary Science*, 54(7), 1594–1603. https://doi.org/10.1111/maps.13299

Muhs, D. R., Simmons, K. R., Schumann, R. R., & Halley, R. B. (2011). Sea-level history of the past two interglacial periods: New evidence from U-series dating of reef corals from south Florida. *Quaternary Science Reviews*, 30(5–6), 570–590. https://doi.org/10.1016/j.quascirev.2010.12.019

Mylroie, J. E., Carew, J. L., & Moore, A. I. (1995). Blue holes: Definition and genesis. *Carbonates and Evaporites*, 10(2), 225–233. https://doi.org/10.1007/BF03175407

Neal, A., Grasmueck, M., McNeill, D. F., Viggiano, D. A., & Eberli, G. P. (2008). Full-resolution 3D radar stratigraphy of complex oolitic sedimentary architecture: Miami Limestone, Florida, U.S.A. *Journal of Sedimentary Research*, 78(9), 638–653. https://doi.org/10.2110/jsr.2008.070

NOAA (National Oceanic and Atmospheric Administration, Office of Coast Survey) (1997). *Descriptive Report to Accompany Hydrographic Survey H-10748, Approaches to Miami, Florida*. Silver Spring, MD.

NOAA CO-OPS (Center for Operational Oceanographic Products and Services) (2020). *Station 8723214 (Virginia Key, Biscayne Bay, FL): Published Tidal Datums (1983–2001 NTDE) and Verified 6-Minute Water Levels (27 June 2020)*. National Oceanic and Atmospheric Administration.

NOAA NGS (National Geodetic Survey) (2017). *2017 NOAA NGS Topobathy Lidar DEM: Fort Lauderdale to Miami, FL (Mission ID 8728)*. NOAA Office for Coastal Management Digital Coast.

NOAA NGS (National Geodetic Survey) (2019). *2018–2019 NOAA NGS Topobathy Lidar DEM Hurricane Irma: Miami to Marquesas Keys, FL (Mission ID 9060)*. NOAA Office for Coastal Management Digital Coast.

NOAA Ocean Exploration (2020). *Exploration of the Gulf of Mexico's Deep-Sea "Blue Holes" (Amberjack Hole and Green Banana Hole)*. National Oceanic and Atmospheric Administration (https://oceanexplorer.noaa.gov/expedition/20blue-holes/).

Ormö, J., & Lindström, M. (2000). When a cosmic impact strikes the sea bed. *Geological Magazine*, 137(1), 67–80. https://doi.org/10.1017/S0016756800003538

Ormö, J., Shuvalov, V. V., & Lindström, M. (2002). Numerical modeling for target water depth estimation of marine-target impact craters. *Journal of Geophysical Research: Planets*, 107(E12), 5120. https://doi.org/10.1029/2002JE001865

Ormö, J., Raducan, S. D., Housen, K. R., Wünnemann, K., Collins, G. S., Rossi, A. P., & Melero-Asensio, I. (2024). Effect of target layering in gravity-dominated cratering in nature, experiments, and numerical simulations. *Journal of Geophysical Research: Planets*, 129(5), e2023JE008110. https://doi.org/10.1029/2023JE008110

Osinski, G. R., Spray, J. G., & Grieve, R. A. F. (2008). Impact melting in sedimentary target rocks: An assessment. In K. R. Evans, J. W. Horton Jr., D. T. King Jr., & J. R. Morrow (Eds.), *The Sedimentary Record of Meteorite Impacts* (Geological Society of America Special Paper 437, pp. 1–18). https://doi.org/10.1130/2008.2437(01)

Osmond, J. K., Carpenter, J. R., & Windom, H. L. (1965). Th^{230}/U^{234} age of the Pleistocene corals and oolites of Florida. *Journal of Geophysical Research*, 70(8), 1843–1847. https://doi.org/10.1029/JZ070i008p01843

Paris, A. J., Robertson, R., & Schwartz, S. (2020). Proposed Miami impact crater identified as a solutional doline of oolictic limestone. *Journal of the Washington Academy of Sciences*, 106(3), Fall 2020. Author manuscript, arXiv:2007.06420.

Patin, N. V., Dietrich, Z. A., Stancil, A., Quinan, M., Beckler, J. S., Hall, E. R., Culter, J., Smith, C. G., Taillefert, M., & Stewart, F. J. (2021). Gulf of Mexico blue hole harbors high levels of novel microbial lineages. *The ISME Journal*, 15(8), 2206–2232. https://doi.org/10.1038/s41396-021-00917-x

Perkins, R. D. (1977). Depositional framework of Pleistocene rocks in south Florida. In P. Enos & R. D. Perkins (Eds.), *Quaternary Sedimentation in South Florida* (Geological Society of America Memoir 147, pp. 131–198). https://doi.org/10.1130/MEM147-p131

Pierazzo, E., & Melosh, H. J. (2000). Hydrocode modeling of oblique impacts: The fate of the projectile. *Meteoritics & Planetary Science*, 35(1), 117–130. https://doi.org/10.1111/j.1945-5100.2000.tb01979.x

Pike, R. J. (1985). Some morphologic systematics of complex impact structures. *Meteoritics*, 20(1), 49–68. https://doi.org/10.1111/j.1945-5100.1985.tb00846.x

Pilkington, M., & Grieve, R. A. F. (1992). The geophysical signature of terrestrial impact craters. *Reviews of Geophysics*, 30(2), 161–181. https://doi.org/10.1029/92RG00192

Poelchau, M. H., Winkler, R., Kenkmann, T., Wirth, R., Luther, R., & Schäfer, F. (2025). Extreme twin densities in calcite—A shock indicator. *Geology*, 53(3), 279–283. https://doi.org/10.1130/G52795.1

Prieur, N. C., Rolf, T., Luther, R., Wünnemann, K., Xiao, Z., & Werner, S. C. (2017). The effect of target properties on transient crater scaling for simple craters. *Journal of Geophysical Research: Planets*, 122(8), 1704–1726. https://doi.org/10.1002/2017JE005283

Prieur, N. C., Rolf, T., Wünnemann, K., & Werner, S. C. (2018). Formation of simple impact craters in layered targets: Implications for lunar crater morphology and regolith thickness. *Journal of Geophysical Research: Planets*, 123(6), 1555–1578. https://doi.org/10.1029/2017JE005463

Quaide, W. L., & Oberbeck, V. R. (1968). Thickness determinations of the lunar surface layer from lunar impact craters. *Journal of Geophysical Research*, 73(16), 5247–5270. https://doi.org/10.1029/JB073i016p05247

Reynolds, G. G. (2009). *Descriptive Report to Accompany Hydrographic Survey H11898, Project OPR-H328-OS-08-C, Approaches to Miami, Florida, March 17 – July 6, 2009* (Ocean Surveys, Inc., 35 pp.; 165 pp. with appendices, plus H11898_MB_1m_MLLW_2of5.bag, H11898_Rky_Area_North, and H11898_Spoil_Area_North). NOAA Office of Coast Survey, Silver Spring, MD.

Roberson, D. S. (1972). *The Paleoecology, Distribution and Significance of Circular Bioherms in the Edwards Limestone of Central Texas* (*Baylor Geological Studies Bulletin*, No. 23, 35 pp.). Baylor University.

Rochette, P., Sagnotti, L., Bourot-Denise, M., Consolmagno, G., Folco, L., Gattacceca, J., Osete, M. L., & Pesonen, L. (2003). Magnetic classification of stony meteorites: 1. Ordinary chondrites. *Meteoritics & Planetary Science*, 38(2), 251–268. https://doi.org/10.1111/j.1945-5100.2003.tb00263.x

Rochette, P., Gattacceca, J., Bonal, L., Bourot-Denise, M., Chevrier, V., Clerc, J.-P., Consolmagno, G., Folco, L., Gounelle, M., Kohout, T., Pesonen, L., Quirico, E., Sagnotti, L., & Skripnik, A. (2008). Magnetic classification of stony meteorites: 2. Non-ordinary chondrites. *Meteoritics & Planetary Science*, 43(5), 959–980. https://doi.org/10.1111/j.1945-5100.2008.tb01092.x

Seybold, L., Trepmann, C. A., Hölzl, S., Pollok, K., Langenhorst, F., Dellefant, F., & Kaliwoda, M. (2023). Twinned calcite as an indicator of high differential stresses and low shock pressure conditions during impact cratering. *Meteoritics & Planetary Science*, 58(9), 1287–1305. https://doi.org/10.1111/maps.14056

Spencer, J. E., Wenrich, K. J., & Cole, T. (2015). *Partial Database for Breccia Pipes and Collapse Features on the Colorado Plateau, Northwestern Arizona* (Digital Information DI-42). Arizona Geological Survey.

Taylor Engineering, Inc. (2021). *Florida Peninsular Sand Source Investigation: Investigation Report Offshore Miami-Dade County* (April 2021; StudyID: USACE_M20PG00014_StateWaters). Prepared for U.S. Army Corps of Engineers, Jacksonville District / Bureau of Ocean Energy Management.

Terho, M., Pesonen, L. J., Kukkonen, I. T., & Bukovanská, M. (1993). The petrophysical classification of meteorites. *Studia Geophysica et Geodaetica*, 37(1), 65–82. https://doi.org/10.1007/BF01613921

Tihansky, A. B. (1999). Sinkholes, west-central Florida. In D. Galloway, D. R. Jones, & S. E. Ingebritsen (Eds.), *Land Subsidence in the United States* (U.S. Geological Survey Circular 1182, pp. 121–140).

Trang, D., Gillis-Davis, J. J., & Hawke, B. R. (2016). The origin of lunar concentric craters. *Icarus*, 278, 62–78. https://doi.org/10.1016/j.icarus.2016.06.001

USACE (U.S. Army Corps of Engineers, Jacksonville District) (1973). *Miami Harbor, Florida, 36-Ft. / 38-Ft. Deepening Project Engineering Plan (River and Harbor Act of August 13, 1968, P.L. 90-483), Sheet 1* (Ref L-1035(73) / Bp 84508-16, compiled onto NOAA Chart 11468 on August 24, 1973).

USACE (U.S. Army Corps of Engineers, Jacksonville District) (2004). *Miami Harbor Navigation Improvements, Miami-Dade County, Florida: Final General Reevaluation Report and Environmental Impact Statement (GRR/EIS)* (constructed 2013–2015).

USACE / FEMA (2017). *2017 FEMA/USACE Post-Irma Topobathy Lidar DEM: Florida (Mission ID 8388)*. Joint Airborne Lidar Bathymetry Technical Center of Expertise, NOAA Digital Coast.

USACE / JALBTCX (2016). *2016 USACE NCMP Topobathy Lidar DEM: Florida East Coast (Mission ID 6196)*. NOAA Digital Coast.

USC&GS (U.S. Coast and Geodetic Survey) (1919). *Descriptive Report to Accompany Hydrographic Survey H-4088a (and H-4075), Biscayne Bay and Approaches, Florida*. U.S. Department of Commerce.

USC&GS (U.S. Coast and Geodetic Survey) (1928). *Descriptive Report to Accompany Hydrographic Survey H-4801, Vicinity of Miami, Florida*. U.S. Department of Commerce.

USC&GS (U.S. Coast and Geodetic Survey) (1935). *Descriptive Report and Review to Accompany Hydrographic Survey H-5727, Approaches to Miami Harbor, Florida (1934–1935)*. U.S. Department of Commerce. https://data.ngdc.noaa.gov/platforms/ocean/nos/coast/H04001-H06000/H05727/DR/H05727.pdf#page=20

Walker, B. K. (2009). *Benthic Habitat Mapping of Miami-Dade County: Visual Interpretation of LADS Bathymetry and Aerial Photography*. Florida Department of Environmental Protection, habitat interpretation south of Government Cut, p. 9. https://floridadep.gov/sites/default/files/LBSP_08_Phase_I_2.pdf

Taylor Engineering (2021). *SAD-SAND Miami-Dade County Investigation Report*. U.S. Army Corps of Engineers, Jacksonville District, April 2021. https://geospatial-data.sec.usace.army.mil/SACS/SAND/References/SAJ/FINAL_SAND_Investigation_Report_MiamiDadex.pdf

USEPA (U.S. Environmental Protection Agency) (1995). Ocean Dumping; Final Designation of Site (Miami Ocean Dredged Material Disposal Site [ODMDS], Florida). *Federal Register*, 60 FR 50108–50114 (40 CFR § 228.15(h)(19)).

Waltham, T., Bell, F. G., & Culshaw, M. G. (2005). *Sinkholes and Subsidence: Karst and Cavernous Rocks in Engineering and Construction* (382 pp.). Springer-Praxis.

Wünnemann, K., Collins, G. S., & Melosh, H. J. (2006). A strain-based porosity model for use in hydrocode simulations of impacts and implications for transient crater growth in porous targets. *Icarus*, 180(2), 514–527. https://doi.org/10.1016/j.icarus.2005.10.013

Wünnemann, K., Weiss, R., & Hofmann, K. (2007). Characteristics of oceanic impact-induced large water waves—Re-evaluation of the tsunami hazard. *Meteoritics & Planetary Science*, 42(11), 1893–1903. https://doi.org/10.1111/j.1945-5100.2007.tb00548.x

Wünnemann, K., Nowka, D., Collins, G. S., Elbeshausen, D., & Bierhaus, M. (2008). Scaling of impact crater formation on planetary surfaces—Insights from numerical modeling. In *Proceedings of the 11th Hypervelocity Impact Symposium* (pp. 1–16).